GEOPHYSICS, VOL. 87, NO. 6 (NOVEMBER-DECEMBER 2022); P. M275–M292, 25 FIGS., 5 TABLES.
10.1190/GEO2021-0631.1

A matrix-fracture-fluid decoupled PP reflection coefficient approximation for seismic inversion in tilted transversely isotropic media

Guangtan Huang[1], Jing Ba[2], Davide Gei[3], and José M. Carcione[3]

ABSTRACT

Fracture-induced azimuthal anisotropy of seismic waves has useful applications in the characterization of hydrocarbon reservoirs as well as the overburden. Existing theories face problems estimating the fracture-weakness parameters, identifying the saturating fluid, and constraining the depth model building. To overcome these problems, we have adopted an azimuthal amplitude variation with angle/offset inversion for the estimation of these parameters and identification of the fluid. First, we define more intuitive fracture and fluid indicators based on rock physics, identifying the fluid by decoupling the fracture weakness parameters. Then, we derive a "rock matrix-fracture-fluid" decoupled PP-wave reflection coefficient approximation of a weakly tilted transversely isotropic medium by using a perturbation matrix and scattering theory. Compared with the conventional fracture weakness-based approximation, our method incorporates the fracture density and the fluid indicator. The inversion test finds that our approximation is effective.

INTRODUCTION

Fractures play an important role in hydrocarbon storage and fluid migration (seepage channels in carbonate or shale reservoirs) (Crampin, 1984; Hsu and Schoenberg, 1993; Bakulin et al., 2000a, 2000b; Carcione et al., 2012b, 2013; Carcione and Picotti, 2012a; Oh and Alkhalifah, 2016). Moreover, their distribution is closely related to the underground stress, which affects the later stage of fracturing development (Hornby et al., 1994; Chen et al., 2017). A reliable prediction of the area of this development and accurate identification of the saturating fluid are important in the petroleum exploration industry.

Propagation of seismic waves in fractured reservoirs usually shows significant anisotropy, so the conventional isotropy theory is no longer satisfied (Rüger, 1997, 1998). Henneke (1972) and Keith and Crampin (1977) first discuss reflection and transmission in anisotropic media. Then, Daley and Hron (1977) derive an analytical solution for the reflection and transmission coefficients of transverse isotropy media with a vertical axis of symmetry (VTI). Based on anisotropy parameters, Schoenberg and Protazio (1990) derive a reflection coefficient for anisotropic media by extending the Zoeppritz equation, but the corresponding expression is nonlinear and not easily amenable for seismic inversion. Graebner (1992) shows that reflectivity methods are difficult to linearize and obtains reflection and transmission coefficients for two transversely isotropic (TI) solids in welded contact. Rüger (1997) derives a weak-anisotropy approximation of the PP reflection coefficient for the medium containing vertical fractures (transverse isotropy with a horizontal axis of symmetry [HTI]), which has been used for fracture prediction. Jílek (2002) obtains the PS-wave reflection coefficient for a TI medium.

Unlike in isotropic or VTI media, wave amplitude in HTI or tilted transverse isotropy (TTI) media depends not only on the incidence angle but also on the azimuth angle. Therefore, the concept of azimuthal anisotropy is essential to characterize fractured reservoirs. Bachrach et al. (2009) propose an amplitude variation with angle and azimuth (AVAZ) attribute extraction method to obtain fracture-related information. Chen et al. (2015) obtain the azimuthal variation of elastic impedance for vertical fractures and establish an inversion method for predicting fracture areas and identifying fluids based on prestack gathers. Furthermore, to improve the accuracy of this method, Chen et al. (2017, 2018) implement subtractions of seismic-data responses from different azimuths and combine them with rock-physics simulations. Using the linear-slip model (Schoenberg and Sayers, 1995), Pan et al. (2018) propose

Manuscript received by the Editor 24 September 2021; revised manuscript received 22 June 2022; published ahead of production 21 August 2022; published online 30 September 2022.
[1]Chinese Academy of Sciences, Institute of Rock and Soil Mechanics, State Key Laboratory of Geomechanics and Geotechnical Engineering, Wuhan, China.
[2]Hohai University, School of Earth Sciences and Engineering, Nanjing, China. E-mail: jba@hhu.edu.cn (corresponding author).
[3]National Institute of Oceanography and Applied Geophysics – OGS, Trieste, Italy.

linearized reflection coefficients for orthorhombic media and show that the fracture weaknesses are appropriate to characterize fracture-induced anisotropy.

However, the aforementioned studies are based on the horizontal layers, but this is not a common situation (Liang et al., 2011; Ivanov and Stovas, 2017), because due to tectonic stresses, particularly in deep reservoirs, the strata often present a large dip. Then, the formations cannot be described as VTI or HTI medium but as TTI. Behura and Tsvankin (2006) provide a small-angle reflection coefficient approximation for TTI media based on the weak-contrast and weak-anisotropy hypothesis. Wang et al. (2017) obtain a P- and S-wave AVAZ approximation for TTI media and analyze the amplitude variation with offset (AVO). Jin and Stovas (2020) derive an S-wave traveltime approximation for a 2D TTI medium. Chen et al. (2020) and Pan et al. (2021) propose a linearized TTI approximation and exploit it as a forward operator to extract fracture weaknesses in tight sandstone reservoirs. For the purpose of fracture and fluid identification, Chen et al. (2014) and Pan et al. (2019a, 2019b) propose the Russell fluid approximation (Russell et al., 2011) and use the isotropic part of the reflection coefficient. However, the anisotropic part of this coefficient is mainly relevant for his purpose.

The aforementioned work mainly focuses on the inversion of the anisotropy parameters or fracture weaknesses. Here, we establish a mapping between fracture parameters and seismic data, and we propose to extract these parameters from the seismic data directly.

Table 1. List of symbols.

Δ	Perturbation	ω	Angular frequency
λ, μ	Lamé parameters	$\mathbf{C}$	Stiffness matrix
K	Bulk modulus	M	P-wave modulus
E	Young's modulus	ν	Poisson's ratio
c	Stiffness component	ρ	Density
c^b	Stiffness component of the background medium	ρ^b	Density of the background medium
$\mathbf{u}^b$	Background wavefield	$\mathbf{u}^s$	Scattering wavefield
x_s	Source location	x'	Observation point
r_0	Stationary point	$\mathbf{B}$	Bond matrix
α	P-wave velocity	β	S-wave velocity
R_{PP}	P-P-wave reflection coefficient	$R_{\mathrm{PP}}^{\mathrm{iso}}$	Isotropic part of R_{PP}
$R_{\mathrm{PP}}^{\mathrm{ani}}$	Anisotropic part of R_{PP}	θ_0	Tilt angle of TTI medium
θ	Incidence angle	ϕ	Azimuthal angle
ζ	μ/M	γ	λ/M
e	Fracture density	χ	Aspect ratio of fracture
Z_N, Z_T	Fracture compliance	δ_N, δ_T	Fracture weakness
$\sigma_v, \sigma_H, \sigma_h$	Stress component	$\mathbf{p}$	Slowness vector
$\mathbf{T}$	Wave vector	ς	Seismic dip
W	Wavelet	$\mathbf{W}$	Wavelet matrix
$\mathbf{S}$	Seismic data	$\Delta\mathbf{S}$	Azimuth difference data
F_p	Russell fluid indicator	F_c	Fluid indicator of the cracks

To improve the seismic inversion, we decouple the effects of the fracture parameters and fluid on the reflection coefficient. We use the thin coin-shaped fracture and linear-slip models (Hudson, 1981; Schoenberg and Sayers, 1995), by which more intuitive fracture and fluid indicators are established, and based on the Russell fluid approximation and scattering theory, we propose a "matrix-fracture-fluid" decoupled reflection coefficient approximation for TTI media to perform the seismic inversion.

METHODOLOGY

Linearized reflection coefficient

In the presence of weak anisotropy, the stiffness components c_{ijkl} and density ρ on a weak-contrast interface can be perturbed with respect to a reference (or background) medium. Table 1 compiles the list of symbols to be used throughout this paper. According to a Taylor expansion, when the perturbations are small, i.e., $|\Delta c_{ijkl}/c_{ijkl}| \ll 1$ and $|\Delta\rho/\rho| \ll 1$, the stiffness components and density can be expressed as (Chapman and Coates, 1994)

$$\rho = \rho^b + \Delta\rho, \quad c_{ijkl} = c^b_{ijkl} + \Delta c_{ijkl}, \quad (i,j,k,l = 1,2,3), \tag{1}$$

where c^b and ρ^b denote the stiffness components and density of the background medium, respectively, and Δ small perturbation from background values. Therefore, based on the scattering theory (Cerveny, 2001), the total wavefield can be decomposed into two parts, namely, the background wavefield $\mathbf{u}^b$ and the scattering wavefield $\mathbf{u}^s$. This can be expressed in the frequency domain as

$$-u_i^s = \Delta\rho\omega^2 u_i^b + \Delta c_{ijkl}\frac{\partial u_k^b}{\partial x_j \partial x_l}, \tag{2}$$

where ω is the angular frequency and u_i^b and u_i^s denote the ith components of the background and scattering displacements, respectively. Because the field is generated at $\mathbf{x}_s$, we have the Green function $\mathbf{G}$ at an observation point $\mathbf{x}'$ (Eaton and Stewart, 1994; Burridge et al., 1998):

$$\mathbf{u}^b(\mathbf{x}', \omega; \mathbf{x}_s) = \mathbf{G}(\mathbf{x}', \omega; \mathbf{x}_s) = \frac{1}{4\pi\rho^b(\alpha^b)^2\mathbf{r}} e^{\mathrm{i}\omega\mathbf{r}/\alpha^b}. \tag{3}$$

To linearize the PP reflection coefficients, Shaw and Sen (2004, 2006) use asymptotic ray theory and the method of stationary phase to describe the scattered wavefield:

$$-\mathbf{u}^s(\mathbf{x}', \omega; \mathbf{x}_s) = \frac{1}{4\pi\rho^b(\alpha^b)^2\mathbf{r}} e^{\mathrm{i}\omega\mathbf{r}/\alpha^b} \frac{1}{4\rho^b\cos^2\theta}\mathbf{S}(\mathbf{r}_0), \tag{4}$$

where $\mathbf{r}$ is the source-receiver distance; $\mathbf{r}_0$ represents the stationary point; α^b is the P-wave velocity of the isotropic background medium; θ denotes the incidence angle of the P wave; and $\mathrm{i} = \sqrt{-1}$ and ω are the imaginary number and frequency, respectively. By considering the symmetry of the stress/strain matrix, stress and strain can be expressed as vectors of six components, and the fourth-order tensor $\mathbf{C}$ can be simplified as a 6×6 matrix. Thus,

$$\mathbf{S}(\mathbf{r}_0) = \Delta\rho\xi + \Delta c_{ij}\eta_{ij}, \quad (i,j = 1,2,\cdots,6). \tag{5}$$

DOI:10.1190/geo2021-0631.1

The slowness- and wave-vector-dependent quantities ξ and η are given in Appendix A. Equation 4 can then be written as (Cerveny, 2001)

$$-\mathbf{u}^s(\mathbf{x}', \omega; \mathbf{x}_s) = \mathbf{G}(\mathbf{x}', \omega; \mathbf{x}_s) R_{\mathrm{PP}}(\theta), \tag{6}$$

where R_{PP} is the PP reflection coefficient at an interface, whose upper medium is isotropic or weakly anisotropic and the lower medium is weakly anisotropic. The linearized expression is

$$R_{\mathrm{PP}} = R_{\mathrm{PP}}^{\mathrm{iso}} + R_{\mathrm{PP}}^{\mathrm{ani}}. \tag{7}$$

Here, $R_{\mathrm{PP}}^{\mathrm{iso}}$ is the isotropic part of the reflectivity, which results from the linear approximation of the Zoeppritz equation (Aki and Richards, 1980; Smith and Gidlow, 1987). The anisotropic part is (Shaw and Sen, 2004)

$$R_{\mathrm{PP}}^{\mathrm{ani}} = \frac{1}{4\rho^b \cos^2\theta}(\Delta\rho\xi + \Delta c_{ij}\eta_{ij}), \quad (i,j = 1,2,\cdots,6). \tag{8}$$

Stiffness matrix of TI media

The stiffness matrix of the isotropic background can be expressed in terms of the bulk modulus M^b and Lamé constants λ^b and μ^b as

$$\mathbf{C}^b = \begin{bmatrix} M^b & \lambda^b & \lambda^b & 0 & 0 & 0 \\ \lambda^b & M^b & \lambda^b & 0 & 0 & 0 \\ \lambda^b & \lambda^b & M^b & 0 & 0 & 0 \\ 0 & 0 & 0 & \mu^b & 0 & 0 \\ 0 & 0 & 0 & 0 & \mu^b & 0 \\ 0 & 0 & 0 & 0 & 0 & \mu^b \end{bmatrix} \tag{9}$$

and the stiffness matrix of the VTI medium is (Carcione, 2014)

$$\mathbf{C}^{\mathrm{VTI}} = \begin{pmatrix} c_{11}^v & c_{12}^v & c_{13}^v & 0 & 0 & 0 \\ c_{12}^v & c_{11}^v & c_{13}^v & 0 & 0 & 0 \\ c_{13}^v & c_{13}^v & c_{33}^v & 0 & 0 & 0 \\ 0 & 0 & 0 & c_{44}^v & 0 & 0 \\ 0 & 0 & 0 & 0 & c_{44}^v & 0 \\ 0 & 0 & 0 & 0 & 0 & c_{66}^v \end{pmatrix}, \quad c_{12}^v = c_{11}^v - 2c_{66}^v, \tag{10}$$

where c_{ij}^v are the stiffness components of the VTI medium. The elasticity matrix (equation 10) can be written in terms of the normal and tangential fracture weakness δ_N and δ_T as (Schoenberg and Sayers, 1995; Carcione et al., 2012c; Carcione, 2014)

$$\mathbf{C}^{\mathrm{VTI}} = \begin{pmatrix} M^b(1-(\zeta^b)^2\delta_N) & \lambda^b(1-\zeta^b\delta_N) & \lambda^b(1-\delta_N) & 0 & 0 & 0 \\ \lambda^b(1-\zeta^b\delta_N) & M^b(1-(\zeta^b)^2\delta_N) & \lambda^b(1-\delta_N) & 0 & 0 & 0 \\ \lambda^b(1-\delta_N) & \lambda^b(1-\delta_N) & M^b(1-\delta_N) & 0 & 0 & 0 \\ 0 & 0 & 0 & \mu^b(1-\delta_T) & 0 & 0 \\ 0 & 0 & 0 & 0 & \mu^b(1-\delta_T) & 0 \\ 0 & 0 & 0 & 0 & 0 & \mu^b \end{pmatrix}, \tag{11}$$

where the P- and S-wave moduli M^b and μ^b and the first Lamé constant λ^b can be expressed as

$$M^b = \rho^b(\alpha^b)^2, \quad \mu^b = \rho^b(\beta^b)^2, \quad \lambda^b = M^b - 2\mu^b, \tag{12}$$

where α^b, β^b, and ρ^b denote the P- and S-wave velocities and density, respectively, and $\zeta^b = \mu^b/M^b$.

Then, we can derive the stiffness matrix of the TTI medium by tilting the symmetry axis with a coordinate transformation. Let us denote with θ_0 the angle between the symmetry axis and the vertical direction (the tilt angle), as shown in Figure 1. The gray platelet indicates the set of parallel fractures with a tilt angle, the red platelet denotes the symmetry axis plane of the fractures, and the green reflector plane indicates the seismic wave reflection interface, which cut the fractures. Axis a is the fracture strike, and axes x, y, and z compose the spatial coordinate system. The ϕ_{obs} corresponds to the angle between the observation line and the x-axis and ϕ_{sym} represents the angle between the symmetry and the x-axis. Let us define the Bond matrix (Bond, 1943; Carcione, 2014):

$$\mathbf{B}_{\theta_0} = \begin{pmatrix} \cos^2\theta_0 & 0 & \sin^2\theta_0 & 0 & -\sin 2\theta_0 & 0 \\ 0 & 1 & 0 & 0 & 0 & 0 \\ \sin^2\theta_0 & 0 & \cos^2\theta_0 & 0 & \sin 2\theta_0 & 0 \\ 0 & 0 & 0 & \cos\theta_0 & 0 & \sin\theta_0 \\ \frac{1}{2}\sin 2\theta_0 & 0 & -\frac{1}{2}\sin 2\theta_0 & 0 & \cos 2\theta_0 & 0 \\ 0 & 0 & 0 & -\sin\theta_0 & 0 & \cos\theta_0 \end{pmatrix}. \tag{13}$$

The stiffness matrix of a TTI medium can be obtained by the transformation (Bond, 1943) as

$$\mathbf{C}^{\mathrm{TTI}} = \mathbf{B}_{\theta_0} \cdot \mathbf{C}^{\mathrm{VTI}} \cdot \mathbf{B}_{\theta_0}^T = \begin{pmatrix} c_{11} & c_{12} & c_{13} & 0 & c_{15} & 0 \\ c_{12} & c_{22} & c_{23} & 0 & c_{25} & 0 \\ c_{13} & c_{23} & c_{33} & 0 & c_{35} & 0 \\ 0 & 0 & 0 & c_{44} & 0 & c_{46} \\ c_{15} & c_{25} & c_{35} & 0 & c_{55} & 0 \\ 0 & 0 & 0 & c_{46} & 0 & c_{66} \end{pmatrix}, \tag{14}$$

where we have used the same symbols for simplicity, and

$$c_{ij} = (b_{ik} \cdot c_{kl}^v) \cdot b_{jl}, \quad (i,j,k,l = 1,2,\cdots,6), \tag{15}$$

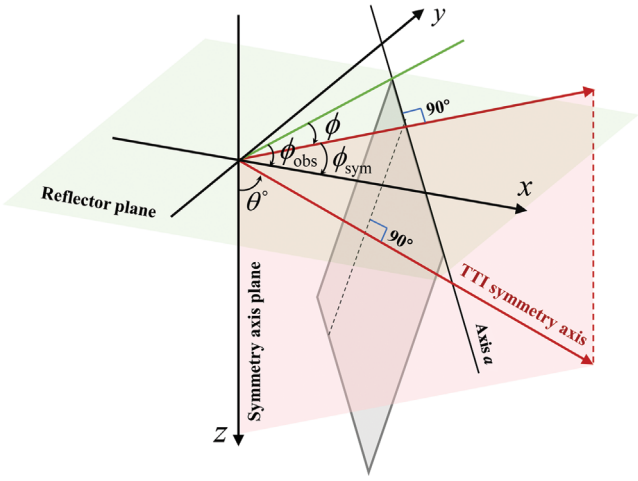

Figure 1. Relationship among the incidence angle θ, tilt angle θ_0, and azimuth angle ϕ. Axis a is the fracture strike, and axes x, y, and z compose the spatial coordinate system. The ϕ_{obs} corresponds to the angle between the observation line and the x-axis and ϕ_{sym} represents the angle between the symmetry and the x-axis.

where b_{ik} is the component of the Bond matrix, and its specific expression can be seen in equation 13.

Based on a weak-anisotropy hypothesis, subtracting $\mathbf{C}^b$ from the $\mathbf{C}^{\mathrm{TTI}}$, we can obtain the perturbations $\Delta\mathbf{C}$. The specific expression of $\Delta\mathbf{C}$ can be found in Appendix B. Then, substituting $\Delta\mathbf{C}$ into equation 8, we obtain the anisotropic part of the PP-wave reflection coefficient:

$$R_{\mathrm{PP}}^{\mathrm{ani}}(\theta,\phi;\theta_0) = k_{\delta_N}(\theta,\phi;\theta_0)\delta_N + k_{\delta_T}(\theta,\phi;\theta_0)\delta_T, \quad (16)$$

where ϕ is the azimuth angle (the difference between the azimuth of the source-receiver line ϕ_{obs} and the horizontal projection of the symmetry axis ϕ_{sym} [Pan et al., 2021]); δ_N and δ_T are given in equations 18 and 19, respectively; and

$$k_{\delta_N}(\theta,\phi;\theta_0) = -\frac{1}{4}\sec^2\theta\left[\begin{array}{l}\cos^4\theta[\gamma^b\cos^2\theta_0(\sin^4\theta+2\sin^2\theta_0)+(\sin^2\theta_0\sin^4\theta+\cos^4\theta_0+(\gamma^b)^2\sin^4\theta_0)]\\ +\gamma^b\sin^4\theta\sin^2\phi(2\gamma^b\cos^2\theta_0\cos^2\phi+2\sin^2\theta_0\cos^2\phi+\gamma^b\sin^2\phi)\\ +[2\gamma^b(\gamma^b\sin^2\theta_0-1)\sin^2\theta_0+(\gamma^b-\frac{1}{2}\sin^2 2\theta_0)]\sin^2\theta\cos^2\theta\cos^2\phi\end{array}\right],$$
$$k_{\delta_T}(\theta,\phi;\theta_0) = \zeta^b\left[\begin{array}{l}(\cos^2 2\theta_0+\cos^2\theta_0-\sin^2\theta_0\tan^2\theta\sin^2\phi-\frac{1}{2}\sin^2 2\theta_0)\sin^2\theta\cos^2\phi\\ -\frac{1}{4}\sin^2 2\theta_0(\sin^2\theta\tan^2\theta\cos^4\phi+\cos^2\theta)\end{array}\right], \quad (17)$$

where $\gamma^b = \lambda^b/M^b$.

Decoupling

The fracture weaknesses related to the infilling medium properties based on the coin-shaped fracture model (Hudson, 1981) and the linear-slip model (Schoenberg and Sayers, 1995) are given by

$$\delta_N = \frac{4e}{3\zeta^b(1-\zeta^b)\left[1+\frac{1}{\pi(1-\zeta^b)}\frac{K'+4/3\mu'}{\mu^b\chi}\right]}, \quad (18)$$

$$\delta_T = \frac{16e}{3(3-2\zeta^b)\left[1+\frac{4}{\pi(3-2\zeta^b)}\frac{\mu'}{\mu^b\chi}\right]}, \quad (19)$$

where K' and μ' denote the bulk and shear moduli of the material filling the fracture, respectively; e is the fracture density; and χ is the aspect ratio of the cracks. Here, the fracture density indicates the average number of fracture intersections per unit length (Narr, 1991) and assumes that the fractures are saturated with a fluid; thus, $\mu' = 0$ and

$$\delta_N = \frac{4e}{3\zeta^b(1-\zeta^b)\left[1+\frac{1}{\pi(1-\zeta^b)}\frac{K'}{\mu^b\chi}\right]} = \frac{4e}{3\zeta^b}\cdot\frac{1}{1-\zeta^b+\frac{K'}{\pi\mu^b\chi}}, \quad (20)$$

$$\delta_T = \frac{16e}{3(3-2\zeta^b)}. \quad (21)$$

Thus, δ_N can be split into the e- and $K'-\chi$-related parts. We assume that the fracture aspect ratio is constant, and ζ^b, related to the background matrix, can be obtained by a conventional amplitude variation with angle (AVA) inversion (Luo et al., 2021) with iterations. We define F_c as the fluid indicator of the cracks,

$$F_c = 1-\zeta^b+\frac{K'}{\pi\mu^b\chi}, \quad (22)$$

which is proportional to the bulk modulus of the fluid filling the fractures. Then,

$$\delta_N = \frac{4e}{3\zeta^b}\cdot\frac{1}{F_c}. \quad (23)$$

For a poroelastic isotropic background where fractures are embedded, equation 16 can be rewritten as

$$R_{\mathrm{PP}}^{\mathrm{ani}}(\theta,\phi;\theta_0) = k_{\delta_N}(\theta,\phi;\theta_0)\frac{4e}{3\zeta^b}\cdot\frac{1}{F_c} + k_{\delta_T}(\theta,\phi;\theta_0)\frac{16e}{3(3-2\zeta^b)}. \quad (24)$$

For an interface separating two media, the upper and lower layers are parameterized by δ_N and δ_T parameters, respectively, wherein $\delta_N = 0$ and $\delta_T = 0$ for isotropic media. One can regard the upper medium as the background of the lower medium. Thus, equation 16 can be expressed as

$$R_{\mathrm{PP}}^{\mathrm{ani}}(\theta,\phi;\theta_0) = k_{\delta_N}(\theta,\phi;\theta_0)\Delta\delta_N + k_{\delta_T}(\theta,\phi;\theta_0)\Delta\delta_T, \quad (25)$$

where $\Delta\delta_N$ and $\Delta\delta_T$ denote the difference of the fracture weaknesses δ_N and δ_T between the upper and lower layers, respectively. The total reflection coefficient is

$$R_{\mathrm{PP}}^{\mathrm{total}}(\theta,\phi;\theta_0) = R_{\mathrm{PP}}^{\mathrm{iso}}(\theta) + k_{\delta_N}(\theta,\phi;\theta_0)\Delta\delta_N + k_{\delta_T}(\theta,\phi;\theta_0)\Delta\delta_T. \quad (26)$$

The perturbations of these parameters can be expressed in differential form, i.e., taking the differential on both sides of equations 20 and 21 as

$$\begin{aligned}\Delta\delta_N &= \delta_N^{\mathrm{lower}} - \delta_N^{\mathrm{upper}} \approx d(\delta_N) = d\left(\frac{4e}{3\zeta^b}\cdot\frac{1}{F_c}\right)\\ &= \frac{4e^{\mathrm{lower}}}{3\zeta^b}\cdot\frac{1}{F_c^{\mathrm{lower}}} - \frac{4e^{\mathrm{upper}}}{3\zeta^b}\cdot\frac{1}{F_c^{\mathrm{upper}}}\\ &= \delta_N^{\mathrm{lower}} r_e - \delta_N^{\mathrm{upper}} r_{F_c},\end{aligned} \quad (27)$$

$$\begin{aligned}\Delta\delta_T &= \delta_T^{\mathrm{lower}} - \delta_T^{\mathrm{upper}} \approx d(\delta_T) = d\left(\frac{16e}{3(3-2\zeta^b)}\right)\\ &= \frac{16e^{\mathrm{lower}}}{3(3-2\zeta^b)} - \frac{16e^{\mathrm{upper}}}{3(3-2\zeta^b)} = \delta_T^{\mathrm{lower}} r_e,\end{aligned} \quad (28)$$

where $r_e = (\Delta e/e^{\mathrm{lower}})$, $r_{F_c} = (\Delta F_c/F_c^{\mathrm{lower}})$, and Δ denotes the perturbation between the upper and lower layers. To prevent

DOI:10.1190/geo2021-0631.1

instability, we assume that the fracture density $e > 0$; otherwise, $\delta_N \to \infty$. Thus, the PP reflection coefficient of the anisotropic part can be written as

$$R_{\mathrm{PP}}^{\mathrm{ani}}(\theta,\phi;\theta_0) = k_e(\theta,\phi;\theta_0)r_e + k_{F_c}(\theta,\phi;\theta_0)r_{F_c}, \quad (29)$$

where

$$\begin{aligned}
&k_e(\theta,\phi;\theta_0)\\
&=-\frac{1}{4}\sec^2\theta\begin{bmatrix}\cos^4\theta[\gamma^b\cos^2\theta_0(\sin^4\theta+2\sin^2\theta_0)+(\sin^2\theta_0\sin^4\theta+\cos^4\theta_0+(\gamma^b)^2\sin^4\theta_0)]\\ +\gamma^b\sin^4\theta\sin^2\phi(2\gamma^b\cos^2\theta_0\cos^2\phi+2\sin^2\theta_0\cos^2\phi+\gamma^b\sin^2\phi)\\ +[2\gamma^b(\gamma^b\sin^2\theta_0-1)\sin^2\theta_0+(\gamma^b-\frac{1}{2}\sin^2 2\theta_0)]\sin^2\theta\cos^2\theta\cos^2\phi\end{bmatrix}\delta_N\\
&+\zeta^b\begin{bmatrix}(\cos^2 2\theta_0+\cos^2\theta_0-\sin^2\theta_0\tan^2\theta\sin^2\phi-\frac{1}{2}\sin^2 2\theta_0)\sin^2\theta\cos^2\phi\\ -\frac{1}{4}\sin^2 2\theta_0(\sin^2\theta\tan^2\theta\cos^4\phi+\cos^2\theta)\end{bmatrix}\delta_T,\\
&k_{F_c}(\theta,\phi;\theta_0)\\
&=\frac{1}{4}\sec^2\theta\begin{bmatrix}\cos^4\theta[\gamma^b\cos^2\theta_0(\sin^4\theta+2\sin^2\theta_0)+(\sin^2\theta_0\sin^4\theta+\cos^4\theta_0+(\gamma^b)^2\sin^4\theta_0)]\\ +\gamma^b\sin^4\theta\sin^2\phi(2\gamma^b\cos^2\theta_0\cos^2\phi+2\sin^2\theta_0\cos^2\phi+\gamma^b\sin^2\phi)\\ +[2\gamma^b(\gamma^b\sin^2\theta_0-1)\sin^2\theta_0+(\gamma^b-\frac{1}{2}\sin^2 2\theta_0)]\sin^2\theta\cos^2\theta\cos^2\phi\end{bmatrix}\delta_N.
\end{aligned} \quad (30)$$

Then, the isotropic part of the PP-wave reflection coefficient is derived as

$$R_{\mathrm{PP}}^{\mathrm{iso}}(\theta) = k_{M^b}(\theta)\frac{\Delta M^b}{M^b} + k_{\mu^b}(\theta)\frac{\Delta\mu^b}{\mu^b} + k_\rho(\theta)\frac{\Delta\rho}{\rho}, \quad (31)$$

where (Pan et al., 2021)

$$k_{M^b}(\theta)=\frac{\sec^2\theta}{4},\quad k_{\mu^b}(\theta)=-2\zeta_{\mathrm{sat}}\sin^2\theta,\quad \text{and}\quad k_\rho(\theta)=\frac{1}{2}-\frac{\sec^2\theta}{4}. \quad (32)$$

The total reflection coefficient is

$$\begin{aligned}
R_{\mathrm{PP}}^{\mathrm{total}}(\theta,\phi,\theta_0) &\approx k_{M^b}(\theta)\frac{\Delta M^b}{M^b} + k_{\mu^b}(\theta)\frac{\Delta\mu^b}{\mu^b} + k_\rho(\theta)\frac{\Delta\rho}{\rho}\\
&+ k_e(\theta,\phi;\theta_0)r_e + k_{F_c}(\theta,\phi;\theta_0)r_{F_c}.
\end{aligned} \quad (33)$$

Moreover, here the isotropic part can be further "matrix-fluid" decoupled. According to Russell et al. (2011), the isotropic part of the PP-wave reflection coefficient is

$$R_{\mathrm{PP}}^{\mathrm{iso}}(\theta) = k_{F_p}(\theta)\frac{\Delta F_p}{F_p} + k_{\mu^b}(\theta)\frac{\Delta\mu^b}{\mu^b} + k_\rho(\theta)\frac{\Delta\rho}{\rho}, \quad (34)$$

where

$$F_p = M_{\mathrm{sat}} - \frac{\mu_{\mathrm{dry}}}{\zeta_{\mathrm{dry}}} \quad (35)$$

is the Russell fluid indicator, and

$$k_{F_p}(\theta)=\left(1-\frac{\zeta_{\mathrm{sat}}}{\zeta_{\mathrm{dry}}}\right)\frac{\sec^2\theta}{4},\quad k_{\mu^b}(\theta)=\frac{\zeta_{\mathrm{sat}}}{\zeta_{\mathrm{dry}}}\frac{\sec^2\theta}{4}-2\zeta_{\mathrm{sat}}\sin^2\theta,$$
$$\text{and}\quad k_\rho(\theta)=\frac{1}{2}-\frac{\sec^2\theta}{4}, \quad (36)$$

where

$$\zeta_{\mathrm{dry}} = \mu_{\mathrm{dry}}/M_{\mathrm{dry}},\quad \zeta_{\mathrm{sat}} = \mu_{\mathrm{sat}}/M_{\mathrm{sat}}. \quad (37)$$

Here, μ_{dry}, μ_{sat} and M_{dry}, M_{sat} are the S- and P-wave moduli of the dry- and wet-rock, respectively. These parameters can be obtained from core and well-log data by using the Gassmann equation (Gassmann, 1951). According to this equation, $\mu_{\mathrm{dry}} = \mu_{\mathrm{sat}}$. Note that F_p is related to the pore fluid in the isotropic background and F_c represents the fracture-fluid indicator. Thus, the total PP-wave reflection coefficient becomes

$$\begin{aligned}
R_{\mathrm{PP}}^{\mathrm{total}}(\theta,\phi;\theta_0) &\approx k_{F_p}(\theta)r_{F_p} + k_{\mu^b}(\theta)r_{\mu^b} + k_\rho(\theta)r_\rho\\
&+ k_e(\theta,\phi;\theta_0)r_e + k_{F_c}(\theta,\phi;\theta_0)r_{F_c},
\end{aligned} \quad (38)$$

where

$$r_{F_p} = \frac{\Delta F_p}{F_p},\quad r_{\mu^b} = \frac{\Delta\mu^b}{\mu^b},\quad \text{and}\quad r_\rho = \frac{\Delta\rho^b}{\rho^b}. \quad (39)$$

We have obtained the reflection coefficient in terms of the parameters of the rock matrix r_{μ^b}, the pore-fluid indicator r_{F_p} and fracture-fluid indicator r_{F_c}, and the fracture parameter r_e, thus achieving a matrix-fracture-fluid decoupling. Here, "matrix" indicates the reflectivity ratio of the shear modulus of the rock matrix r_{μ^b}, "fracture" corresponds to the reflectivity ratio of the fracture density r_e, and "fluid" corresponds to the reflectivity ratios of the pore-fluid indicator r_{F_p} and fracture-fluid indicator r_{F_c}.

Inversion theory

According to the convolutional model, seismic data can be expressed as reflectivity convolved with a seismic wavelet:

$$\mathbf{s}_{\mathrm{PP}}(t;\theta,\phi,\theta_0) = \mathbf{w}(t;\theta,\phi) * \mathbf{r}_{\mathrm{PP}}(t;\theta,\phi,\theta_0), \quad (40)$$

where $\mathbf{w}$ is the incidence- and azimuth-angle-dependent seismic wavelet vector and $\mathbf{s}_{\mathrm{PP}}$ and $\mathbf{r}_{\mathrm{PP}}$ denote the P-P-wave reflectivity and the seismic data vectors. This equation can be rewritten in a matrix form:

$$\mathbf{S}(\theta,\phi;\theta_0) = \mathbf{W}(\theta,\phi)\mathbf{R}_{\mathrm{PP}}(\theta,\phi;\theta_0), \quad (41)$$

where

DOI:10.1190/geo2021-0631.1

$$\mathbf{S}_{\mathrm{PP}}(\theta,\phi,\theta_0)=\begin{bmatrix} s_{\mathrm{PP}}(1,\theta,\phi,\theta_0)\\ s_{\mathrm{PP}}(2,\theta,\phi,\theta_0)\\ \vdots\\ s_{\mathrm{PP}}(i,\theta,\phi,\theta_0)\\ \vdots\\ s_{\mathrm{PP}}(N,\theta,\phi,\theta_0)\end{bmatrix},\quad \mathbf{R}_{\mathrm{PP}}(\theta,\phi,\theta_0)=\begin{bmatrix} R_{\mathrm{PP}}(1,\theta,\phi,\theta_0)\\ R_{\mathrm{PP}}(2,\theta,\phi,\theta_0)\\ \vdots\\ R_{\mathrm{PP}}(i,\theta,\phi,\theta_0)\\ \vdots\\ R_{\mathrm{PP}}(N,\theta,\phi,\theta_0)\end{bmatrix},$$

$$\mathbf{W}(\theta,\phi)=\begin{bmatrix} w(1,\theta,\phi) & w(2,\theta,\phi) & \cdots & w(N,\theta,\phi)\\ w(2,\theta,\phi) & w(3,\theta,\phi) & \cdots & w(1,\theta,\phi)\\ & & \vdots & \\ w(i,\theta,\phi) & w(i+1,\theta,\phi) & \cdots & w(N-i+1,\theta,\phi)\\ & & \vdots & \\ w(N,\theta,\phi) & w(1,\theta,\phi) & \cdots & w(N-1,\theta,\phi)\end{bmatrix}, \quad (42)$$

where i denotes the temporal sample.

As shown in equation 7, the reflection coefficient can be divided into two parts, i.e., an azimuth-dependent anisotropic part $R_{\mathrm{PP}}^{\mathrm{ani}}$ and an azimuth-independent reflection coefficient related to the isotropic part $R_{\mathrm{PP}}^{\mathrm{iso}}$. Thus, based on equation 29, the amplitude difference of seismic data from different azimuths $\Delta\mathbf{S}(\theta,\phi_i,\phi_j;\theta_0)$ can be expressed as

$$\begin{aligned}
&\Delta\mathbf{S}(\theta,\phi_i,\phi_j;\theta_0)\\
&=\mathbf{S}(\theta,\phi_i;\theta_0)-\mathbf{S}(\theta,\phi_j;\theta_0)\\
&=\overline{\mathbf{W}}(\theta,\phi_i,\phi_j)[\mathbf{R}_{\mathrm{PP}}(\theta,\phi_i;\theta_0)-\mathbf{R}_{\mathrm{PP}}(\theta,\phi_j;\theta_0)]\\
&=\overline{\mathbf{W}}(\theta,\phi_i,\phi_j)[\mathbf{R}_{\mathrm{PP}}^{\mathrm{iso}}(\theta)+\mathbf{R}_{\mathrm{PP}}^{\mathrm{ani}}(\theta,\phi_i;\theta_0)-\mathbf{R}_{\mathrm{PP}}^{\mathrm{iso}}(\theta)-\mathbf{R}_{\mathrm{PP}}^{\mathrm{ani}}(\theta,\phi_j;\theta_0)]\\
&=\overline{\mathbf{W}}(\theta,\phi_i,\phi_j)\{[k_e(\theta,\phi_i;\theta_0)-k_e(\theta,\phi_j;\theta_0)]\mathbf{r}_e+[k_{F_c}(\theta,\phi_i;\theta_0)-k_{F_c}(\theta,\phi_j;\theta_0)]\mathbf{r}_{F_c}\},
\end{aligned} \quad (43)$$

where ϕ_i and ϕ_j denote the ith and jth azimuth angles, respectively; and $\overline{\mathbf{W}}(\theta,\phi_i,\phi_j)$ is the average of $\mathbf{W}(\theta,\phi_i)$ and $\mathbf{W}(\theta,\phi_j)$, i.e.,

$$\overline{\mathbf{W}}(\theta,\phi_i,\phi_j)=\frac{1}{2}(\mathbf{W}(\theta,\phi_i)+\mathbf{W}(\theta,\phi_j)); \quad (44)$$

and $\mathbf{r}_e$ and $\mathbf{r}_{F_c}$ denote the reflection ratio vectors of the fracture density and the proposed fluid indicator, respectively, which are

$$\begin{aligned}
\mathbf{r}_e&=[r_e(1),r_e(2),\cdots,r_e(i),\cdots,r_e(N)]^T,\\
\mathbf{r}_{F_c}&=[r_{F_c}(1),r_{F_c}(2),\cdots,r_{F_c}(i),\cdots,r_{F_c}(N)]^T.
\end{aligned} \quad (45)$$

Table 2. Material properties (Wright, 1987).

		V_{11} (km/s)	V_{33} (km/s)	V_{55} (km/s)	V_{13} (km/s)	ρ (g/cm^3)
Upper layer	Shale 1	3.810	3 048	1.219	0.609	2.3
	Shale 2	3.810	3.048	1.219	1.828	2.3
	Shale 3	3.810	3.048	1.219	3.048	2.3
Lower layer	Chalk	5.029	5.029	2.621	3.414	2.7

SENSITIVITY ANALYSIS

Two-layer model analysis

To verify the effectiveness of the proposed approximation, we compare it with the exact solution (Graebner, 1992; Carcione, 2014; Luo et al., 2020), where we use the material properties given in Wright (1987) (see Table 2, $V_{ij}=\sqrt{c_{ij}/\rho}$). The model is composed of an anisotropic shale (VTI medium with different c_{13}) overlying isotropic chalk.

Figure 2 shows the PP reflection coefficients. Figure 2a, 2c, and 2e corresponds to the reflection coefficients by using shales 1, 2, and 3 as upper layers, and chalk as a lower layer. The solid red lines denote the exact solution, the dotted-dashed blue lines are calculated by the Graebner equation (see equation 22 in Graebner, 1992), and the dashed red lines correspond to the proposed approximations (see equation 33). The Graebner solution is consistent with the exact solution when the phase angle does not exceed the critical angle. It is clear that the approximation does not hold for strong anisotropy at far offsets (greater than 30°).

For weak anisotropy, we consider the example given in Table 3. Wood's equation is exploited to mix the fluids (Domenico, 1976) with 90% brine and 10% gas. The properties of the upper and lower layers for the reflectivity simulation are given in Table 3 as well as the fluid modulus. To simplify, we assume that the tilt and azimuth angles are 0°. Then, the exact solution, the Graebner equation (Graebner, 1992; Luo et al., 2020), the Rüger approximation (Rüger, 2002), the fracture weakness-related approximation (equation 16), and the proposed method (equation 33) are used as forward operators to compute the reflection coefficients, as shown in Figure 3. The dotted-dashed red and green lines correspond to the reflection coefficients computed with equations 26 and 33, respectively. The exact and Graebner curves coincide and the other approximations agree fairly well with the exact one, although at large angles there are some discrepancies. The proposed method uses equation 33, but at near-medium angles (less than 30°), the solution is satisfactory.

Then, by perturbing the fracture properties, we analyze the influence of e and fluid type on the fracture weakness based on equations 20 and 21 (see Figures 4 and 5). The matrix properties correspond to the parameters of the upper layer in Table 3. The fractures are saturated with brine (Figure 4a and 4d), oil (Figure 4b and 4e), and gas (Figure 4c and 4f). The fluid modulus significantly affects δ_N but not δ_T. Therefore, the ratio δ_N/δ_T can be considered as a fluid indicator. Moreover, the increase in fracture density increases the fracture weakness and enhances the anisotropy.

Figure 5 shows the influence of χ and saturating fluid. Similar to the fracture density e, χ significantly affects the fracture weaknesses. Moreover, Figure 5 also shows that the fluid modulus affects the anisotropy, in particular, that corresponding to gas-water. Gas-water (or oil-water) indicates that gas (or oil) and brine are

DOI:10.1190/geo2021-0631.1

mixed in the fractures. The water saturation ranges from 0.1 to 0.9, as shown in Figure 5. Such features provide us a basis for subsequent fluid indications, especially for fractured gas reservoirs.

Well-log data test

We consider well-log data and the corresponding fracture parameters are obtained by using the linear-slip model. The data are from southwest China and have been converted to the time domain by using a seismic-well tie. Figure 6 shows the profiles, including the P- and S-wave moduli M^b and μ^b, density ρ, fracture weakness δ_N and δ_T, fracture density e, and fluid indicator. The solid black curves are calculated by using the well-log profiles based on

$$c_{33}=\rho V_{\mathrm{P},0}^2,\quad c_{55}=\rho V_{\mathrm{S},0}^2,\quad c_{11}=\rho V_{\mathrm{P},90}^2,\quad c_{44}=\rho V_{\mathrm{S},90}^2, \tag{46}$$

where $V_{\mathrm{P},0}$, $V_{\mathrm{P},90}$ and $V_{\mathrm{S},0}$, $V_{\mathrm{S},90}$ are the vertical (0°) and horizontal (90°) P- and S-wave velocities, respectively. Then, according to the well logs, especially the resistivity log, we can estimate the tilt angle of the fractures (Liu et al., 2020). The fracture weakness δ_N and δ_T can be obtained from equation B-2 in Appendix B. To simplify, here the fracture density e and aspect ratio χ are obtained based on the Hudson model by assuming the properties of brine given in Table 3 in the inversion test. The P- and S-wave moduli M^b and μ^b are estimated from P- and S-wave velocity, respectively. One can use core data to obtain the dry-rock moduli, porosity, etc., and then compute the pore-fluid indicator F_p based on the Gassmann equation. To

Table 3. Material properties.

	Property	Value
Upper layer	P-wave velocity α_{dry}	3.048 km/s
	S-wave velocity β_{dry}	1.490 km/s
	Bulk density ρ^b	2.420 g/cm^3
	Porosity ϕ	0.05
	Fracture density e	0.1
	Aspect ratio χ	0.09
Lower layer	P-wave velocity α_{dry}	3.483 km/s
	S-wave velocity β_{dry}	2.338 km/s
	Bulk density ρ^b	2.300 g/cm^3
	Porosity ϕ	0.05
	Fracture density e	0.05
	Aspect ratio χ	0.05
Fluid	P-wave velocity α_{brine}	1.47 km/s
	Bulk density ρ_{brine}	1.04 g/cm^3
	P-wave velocity α_{oil}	0.750 km/s
	Bulk density ρ_{oil}	0.70 g/cm^3
	P-wave velocity α_{gas}	0.603 km/s
	Bulk density ρ_{gas}	0.0011 g/cm^3

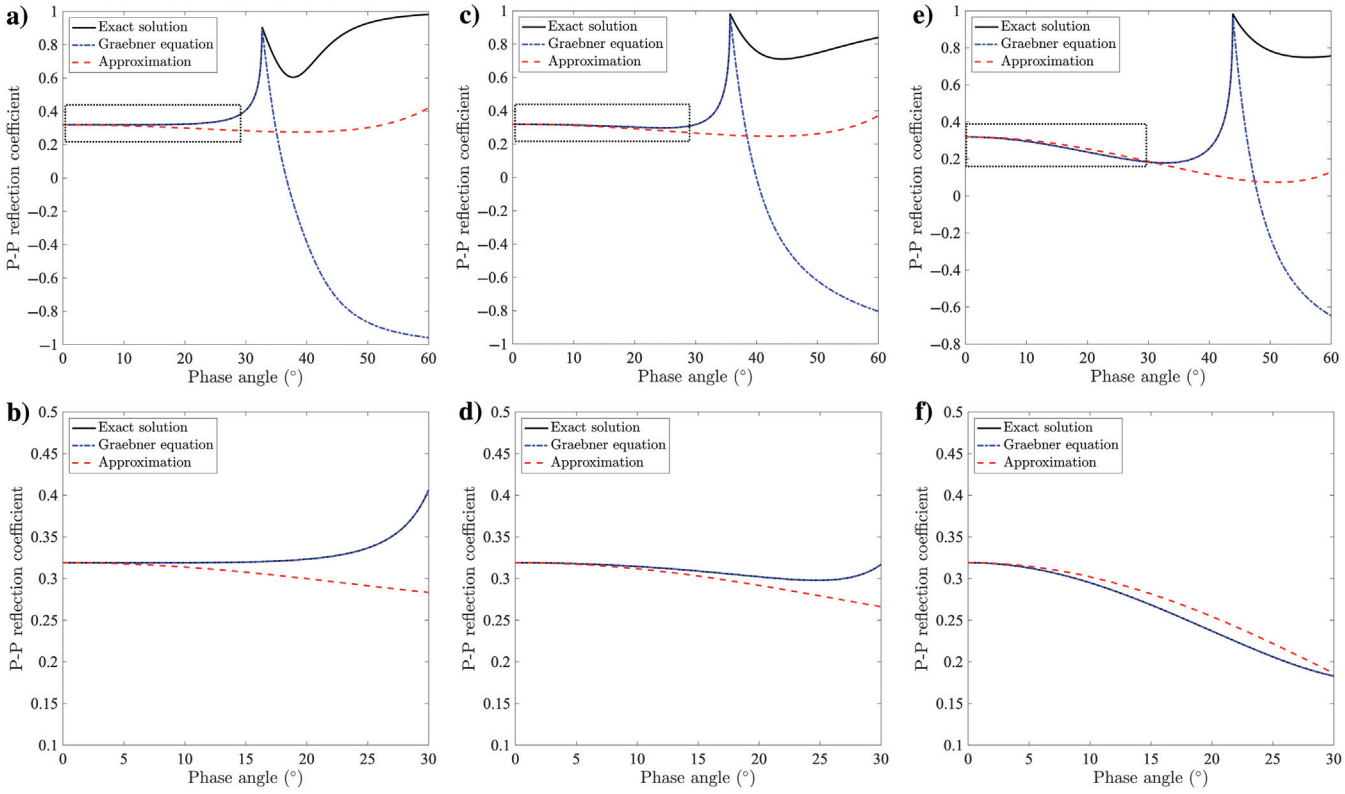

Figure 2. Comparison of the proposed method with (a, c, and e) the exact solution and Graebner equation by using the material properties given in Table 1 and (b, d, and f) the respective magnified results of the comparison in the black boxes.

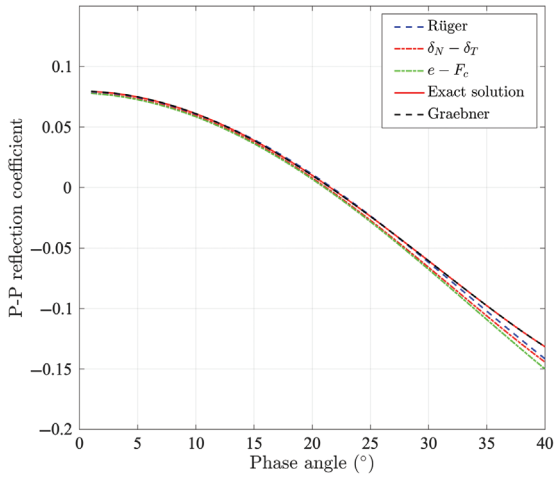

Figure 3. PP reflection coefficients obtained with the exact solution, Graebner equation, Rüger approximation, fracture-weakness-related approximation (equation 26), and proposed method (equation 33).

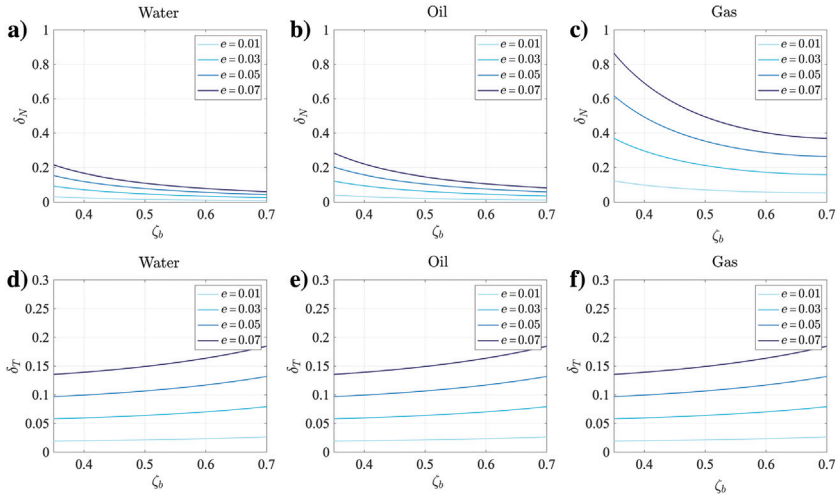

Figure 4. Fracture weaknesses as a function of the fracture density e and fracture-filling property.

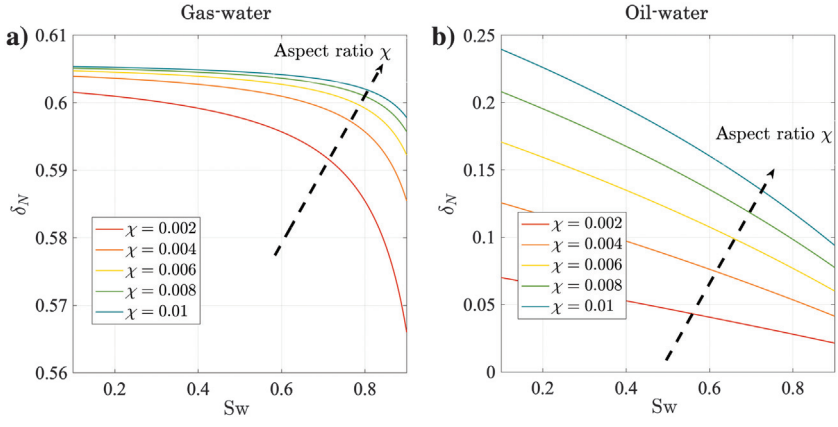

Figure 5. Fracture weaknesses as a function of the fracture aspect ratio χ and fluid modulus.

perform the seismic inversion, we need the tilt angle and initial models as input data and extract the properties of the fractures (e and F_c) and moduli and density of the host rock (M^b, μ^b, and ρ^b) from seismic data. Moreover, we have introduced an indicator factor, which is an important parameter in the shale fracturing process, i.e., the differential horizontal stress ratio (DHSR) (Gray et al., 2012):

$$\mathrm{DHSR} = \frac{\sigma_H - \sigma_h}{\sigma_H} = \frac{E^b Z_N}{1 + E^b Z_N + \nu^b}, \tag{47}$$

where

$$Z_N = \frac{\delta_N}{M^b(1 - \delta_N)} \tag{48}$$

is the normal-fracture compliance. Here, E^b and ν^b denote the Young's modulus and Poisson's ratio of the rock matrix, respectively, i.e.,

$$E^b = \frac{\mu^b(2\zeta^b - 1)}{\zeta^b - 1}, \quad \nu^b = \frac{2\zeta^b - 1}{2(\zeta^b - 1)}. \tag{49}$$

In general, a high DHSR value indicates that a high number of fractures parallel to the maximum horizontal principal stress are developed in the formation. Referring to the fracture density information and DHSR parameters, the fractures that are not parallel to the horizontal stress direction can be somewhat characterized.

As shown in Figure 6, the fractured formation, shale formation, and the fractured shale gas reservoir and limestone formation are sequentially deposited. The two dashed boxes in Figure 6 correspond to the two different fracture systems. It is shown from the fracture density curve (the sixth panel) that there is considerable crack development in both areas. However, the fluid indicator in the cracks F_c (the seventh panel) and the DHSR curves (the eighth panel) show that the two regions have opposite behaviors. The area highlighted in the black box corresponds to a high fracture density, and the high $1/F_c$ value indicates that the fracture is saturated with a low bulk modulus fluid (shale gas). In contrast, the area highlighted in the red box corresponds to a high density but low $1/F_c$ value. The formation is water-saturated, heavily fractured, with a low gas content. Then, the seismic response difference between the two formations should be taken into consideration.

We apply equation 16 to simulate the azimuthal amplitude variation with azimuth by using the well-log data. We have obtained the azimuth-dependent reflection coefficients corresponding to the two formations (see Figures 7 and 8). The parameters to obtain the reflection coefficients are the average of the values within

DOI:10.1190/geo2021-0631.1

the red and black boxes in Figure 6 (see Table 4). The well-log data are used for sensitivity analysis. When we adjust the tilt angle, we only change the dip angle of the fractures. Comparing Figures 7 and 8 shows that, when the tilt angle of the fractures is 0°, which corresponds to a VTI medium, the reflection coefficient is azimuth independent. Increasing this angle, the azimuth effects anisotropy increase; for 90°, we have an HTI medium.

It is necessary to quantitatively extract the fracture and fluid information (Ba et al., 2017; Zhang et al., 2021, 2022). Thus, to extract such information, it is important that the contribution of each parameter to the reflection coefficient (or seismic data) should be similar. A similar sensitivity or contribution of the parameters to the seismic data indicates that the condition number of the forward operator is small. It means that it is less likely to induce ill-posedness. Otherwise, it is easy to induce an ill-posed problem due to the large condition number of the forward operator. As shown in equations 25 and 29, the reflection coefficient is a weighted summation of the parameters to be calculated, and the contribution mainly results from the weights and the parameters. The parameters of the AVAZ inversion are $\Delta\delta_N$ and $\Delta\delta_T$ for equation 25 and r_e and r_{F_c} for equation 29. The balance of weights is an important factor in the stability of the inversion. Therefore, we mainly focus on the contribution of the weights.

We consider the properties in the black box as an example. Figure 9a shows the weights k_{δ_N} and k_{δ_T} appearing in equation 25 as a function of θ, azimuth angle ϕ, and tilt angle, which is set to 60°. It can be seen that these two weights depend on the background properties and also are controlled by the incidence angle and azimuth angles: k_{δ_T} is small and slightly varies with these angles; instead, k_{δ_N} is large and varies drastically. As shown in equation 25, the reflection coefficient is equal to the weighted value of $\Delta\delta_N$ and $\Delta\delta_T$. When k_{δ_N} is large and has a wide range, whereas k_{δ_T} is small and varies smoothly, the weighting result is highly affected by $\Delta\delta_N$. Such difference can easily yield an ill-posed problem in the seismic inversion process (equation 25), i.e., a small perturbation of $\Delta\delta_N$ causes a large change in $\Delta\delta_T$. In particular, the anisotropic part of the reflection coefficient is very small, easily affected by noise and more likely to cause ill-posed problems. Figure 9b shows the weights k_e and k_{F_c} appearing in equation 29, where we can see that their behavior is similar, indicating that the two parameters r_e and r_{F_c} have a contribution similar to the seismic data. There are no high variations of one parameter due to the small perturbation of the other parameter and this reduces the ill-posedness in solving the inverse problem.

The proposed approximation has a balanced parameter contribution. However, k_e and k_{F_c} contain the fracture parameters δ_N and δ_T, which means that those coefficients become model-dependent variables, and the problem becomes a nonlinear iterative inversion. An initial model is required to simulate the initial wavefield, but the weight of the coefficients k_e and k_{F_c} should not be highly dependent on this initial model. Otherwise, it can be difficult to obtain reasonable inversion results.

Next, we verify the dependency of the reflection coefficient on the initial model, which is used to calculate the weights k_e and k_{F_c} and obtain the anisotropic part of the reflection coefficient, as shown in Figure 10, using the exact and smoothed values, respectively. The tilt angle is set to 60°. We use a moving average filtering method to find the smooth values. The moving average filter of vector $\mathbf{x}$ with $N_s = 20$ points filter is given by

$$x_s(i,N_s) = \frac{1}{N_s}\left[x\left(i-\frac{N_s}{2}\right), x\left(i-\frac{N_s}{2}+1\right), \cdots, x(i), \cdots, x\left(i+\frac{N_s}{2}-1\right), x\left(i+\frac{N_s}{2}\right)\right]. \quad (50)$$

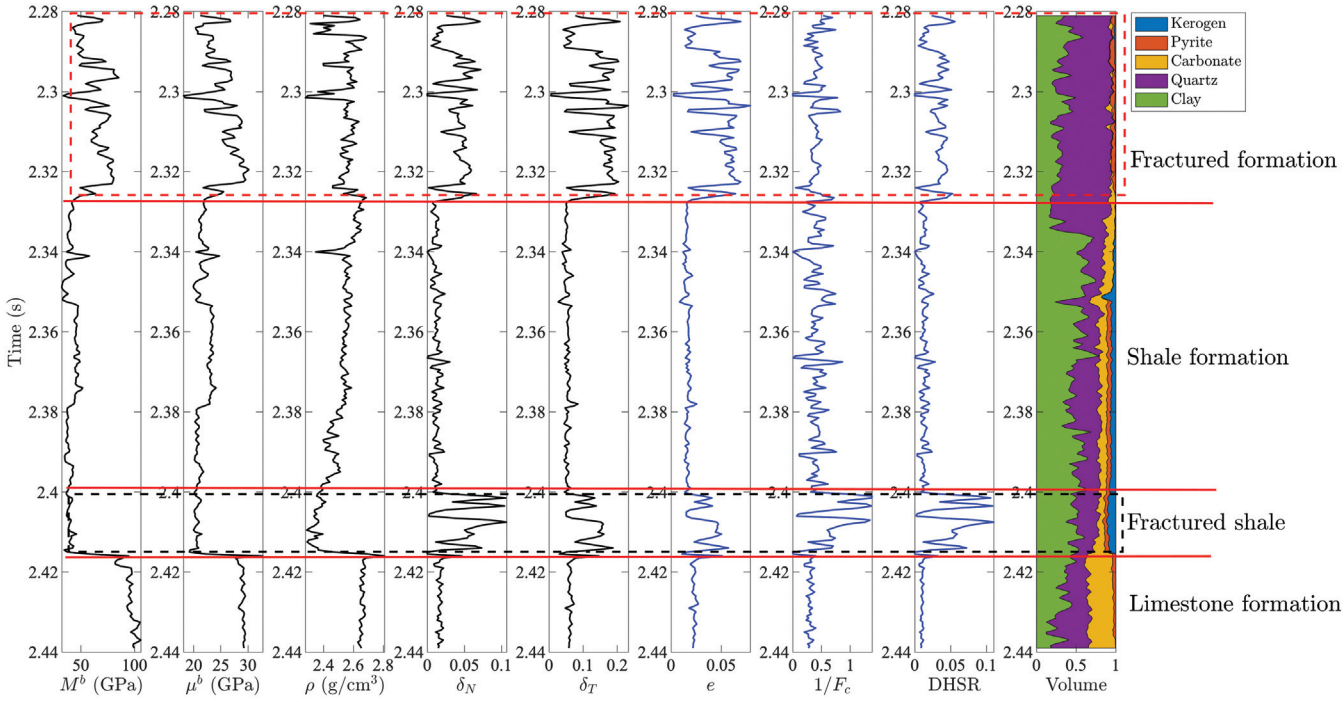

Figure 6. Well-log data, including the P- and S-wave moduli M^b and μ^b, density ρ, fracture weaknesses δ_N and δ_T, fracture density e, DHSR, the fluid indicator in cracks F_c, and volume of minerals. The dashed red and black boxes indicate two fractured areas.

The smoothed models include the moduli of the rock matrix M^b, μ^b, and ρ^b and initial values of the fracture properties e and F_c. It is shown that there is basically no difference between the two sets of results. To further verify the effect of the simulation, we extract the AVAZ at 20° incidence angle and the AVO effect at 90° azimuth angle (see Figure 11). The results show that the approximation does not greatly depend on the initial model.

INVERSION TEST

To check the effectiveness of the numerical implementation, the well-log data in Figure 6 are used for the inversion test, whose workflow is given in Table 5. We neglect the dependency of the wavelet on the incidence and azimuth angles. We use equation 41 to simulate the azimuthal angle gathers as input data, where the incidence angle

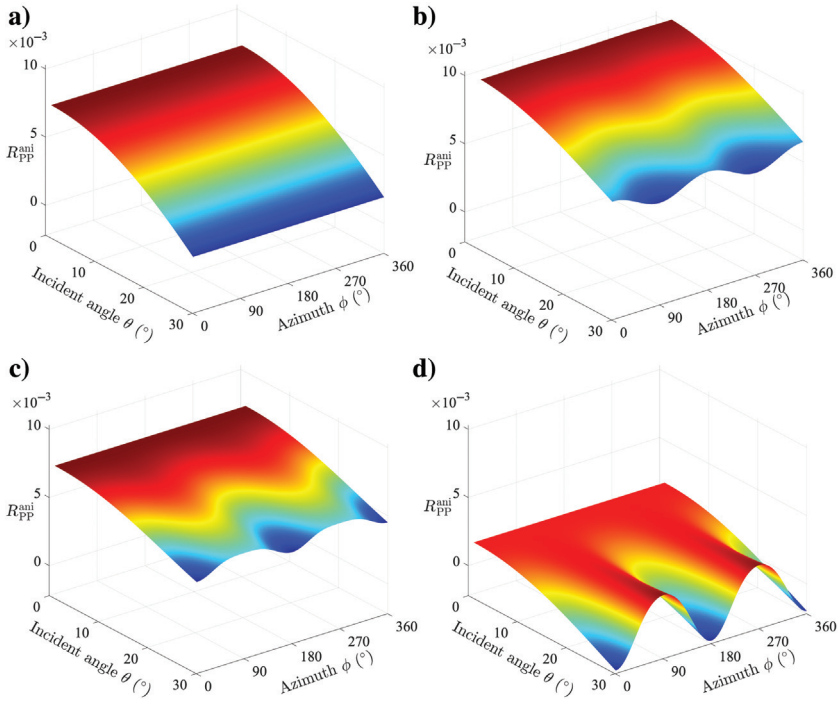

Figure 7 Azimuth-dependent reflection coefficients with tilt angles (a) $\theta_0 = 0°$, (b) $\theta_0 = 30°$, (c) $\theta_0 = 60°$, and (d) $\theta_0 = 90°$, corresponding to the formation of the red box in Figure 6.

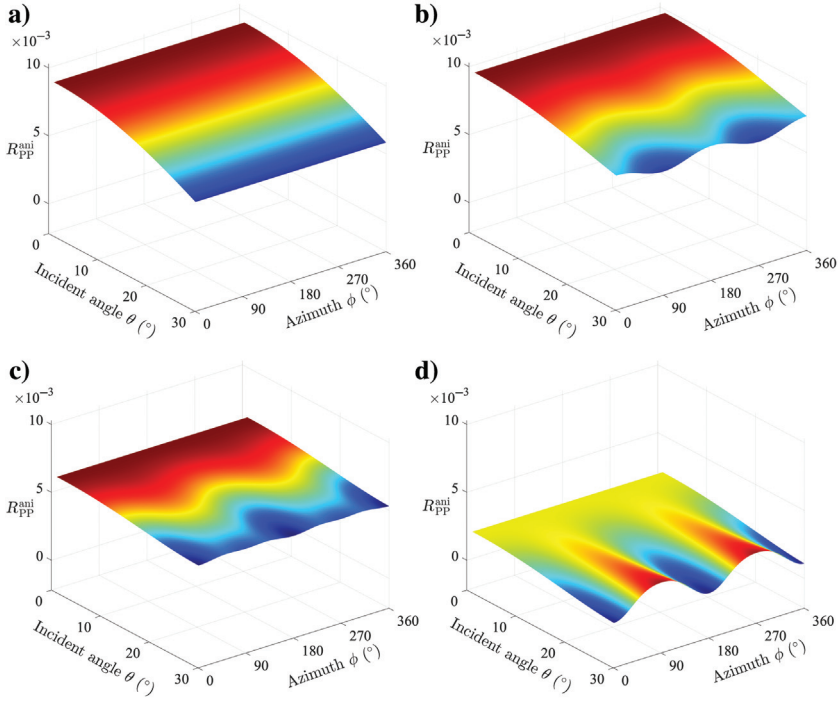

Figure 8. Azimuth-angle-dependent reflection coefficients with tilt angles (a) $\theta_0 = 0°$, (b) $\theta_0 = 30°$, (c) $\theta_0 = 60°$, and (d) $\theta_0 = 90°$, corresponding to the formation of the black box in Figure 6.

DOI:10.1190/geo2021-0631.1

ranges from 0° to 20°, the azimuth angle ranges from 0° to 180°, the tilt angle is set to 60°, and the following Ricker wavelet, with a dominant frequency $f_0 = 30$ Hz, is used for synthesizing seismic data.

$$w(t) = [1 - 2(\pi f_0 t)^2]\exp(-(\pi f_0 t)^2). \quad (51)$$

Figure 12 shows the synthetic azimuthal angle gathers. Then, we obtain the azimuthal-difference data for inverting the target parameters by using equation 29. Figure 13 shows these data, where the difference is mainly present at far-angle ranges; we use the azimuthal-difference data as observed data and provide the smoothed M^b, μ^b, ρ^b, e, and F_c as initial models.

The inversion for a TI medium has several target parameters, which makes the procedure more difficult than that of an isotropic medium. Because the anisotropic and isotropic parts are azimuth-dependent and independent, respectively, the inversion of HTI or TTI medium can be achieved by a two-step algorithm. Based on a Cauchy-norm regularized least-squares inversion strategy (Alemie and Sacchi, 2011), we obtain r_e and r_{F_c}. Figure 14 shows the comparison between the inversion results (the dashed red line) and the input data (the solid blue line). The dashed black line corresponds to the initial model, which is obtained by a moving average filtering with $N_s = 20$. It is shown that the inversion suitably describes the fracture parameters and the proposed fluid indicator. Through a trace-integration algorithm, we can transform the results into model data. Figure 15 shows the transformed fracture density e and the proposed fracture-fluid indicator F_c. The solid blue lines indicate the well-log profiles and the dotted-dashed red lines denote the inverted results. Basically, the inversion results agree with the true values.

Table 4. Properties for azimuth-dependent reflection coefficients calculation.

	Property	Upper layer	Lower layer
Red box	M^b (GPa)	67.0874	41.4517
	μ^b (GPa)	26.1416	21.8647
	ρ^b (g/cm^3)	2.5453	2.5299
	δ_N	0.043	0.0129
	δ_T	0.1517	0.0542
Black box	M^b (GPa)	42.3284	41.4517
	μ^b (GPa)	20.9867	21.8647
	ρ^b (g/cm^3)	2.38	2.5299
	δ_N	0.0495	0.0129
	δ_T	0.1129	0.0542

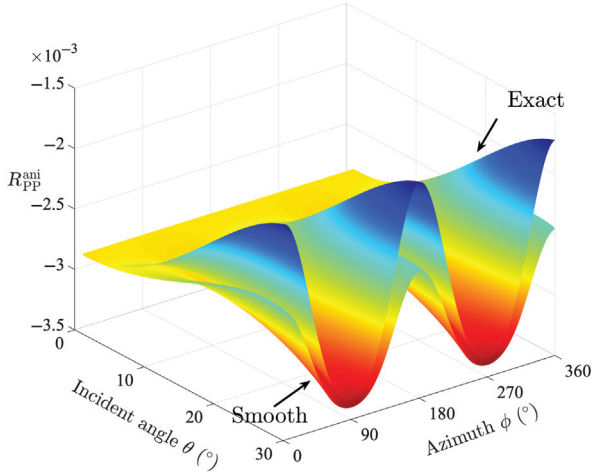

Figure 10. The R_{PP}^{ani} for the exact and smoothed values of k_e and k_{F_c}.

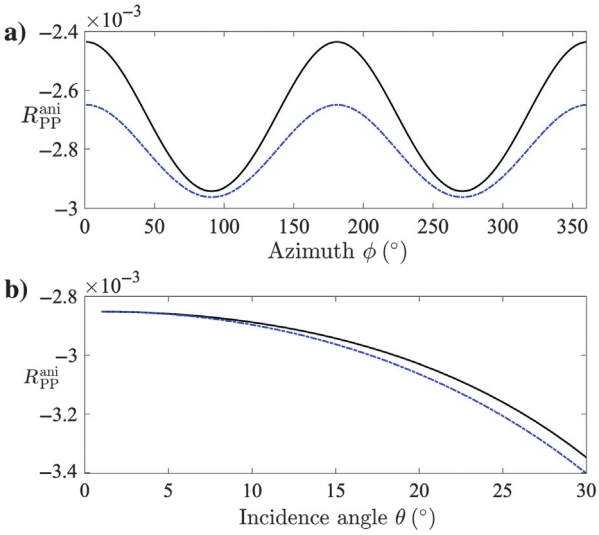

Figure 11. (a) Extracted AVAZ responses (see Figure 9) at 20° incidence angle and (b) AVO at 90° azimuth angle. The solid black and dotted-dashed blue lines are the R_{PP}^{ani} for the exact and smoothed values of k_e and k_{F_c}, respectively.

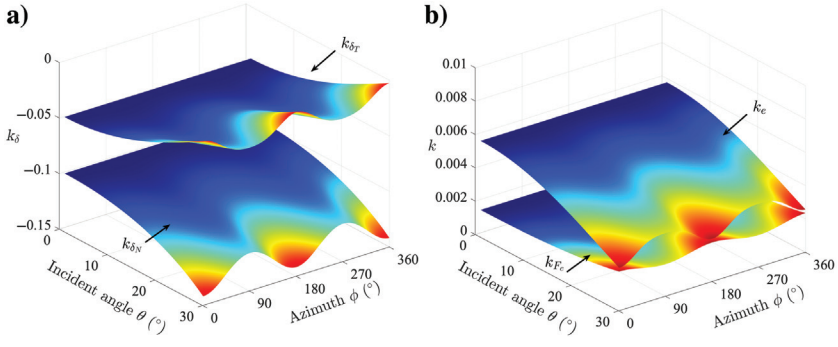

Figure 9. Weights appearing in equations 25 and 29 as a function of the incidence angle θ and azimuth ϕ.

Then, by substituting the inverted r_e and r_{F_c} as known parameters into equation 33, the inversion results of the isotropic part of the reflection coefficient are obtained. The process is similar to the inversion of isotropic media and does not require updating r_e and r_{F_c}. Figure 16 shows the inverted r_{M^b}, r_{μ^b}, and r_ρ of the background medium. The results compare well with the input well-log data. Basically, highly accurate inversions of r_e and r_{F_c} will lay a solid foundation for subsequent inversions.

Finally, by using a trace integral algorithm, M^b, μ^b, and ρ can be obtained for the reservoir characterization, as shown in Figure 17. Let us consider how the ratio r_{M^b} transforms to M^b (Huang et al., 2019). We have

$$\mathbf{r}_{M^b}(t_i) = \frac{M^b(t_{i+1}) - M^b(t_i)}{M^b(t_{i+1}) + M^b(t_i)}. \tag{52}$$

Table 5. Workflow of the AVAZ inversion by using the decoupled approximation.

Input: initial model and azimuthal prestack angle gather seismic data
Output: fracture density and fluid indicator
1. **Execution** of the subtraction process and azimuthal difference data.
2. **Simulation** of the azimuthal difference synthetic data by using equation 29 with initial models.
3. **Estimation** of r_e and r_{F_c} of the fracture reservoir by using a Cauchy-norm regularized least-squares algorithm.
4. **Substitution** of the inversion result r_e and r_{F_c} into equation 33 and calculation of the isotropic part of the elastic-parameter ratios.
5. **Execution** of the trace integral process to transform the reflectivities to elastic parameters.

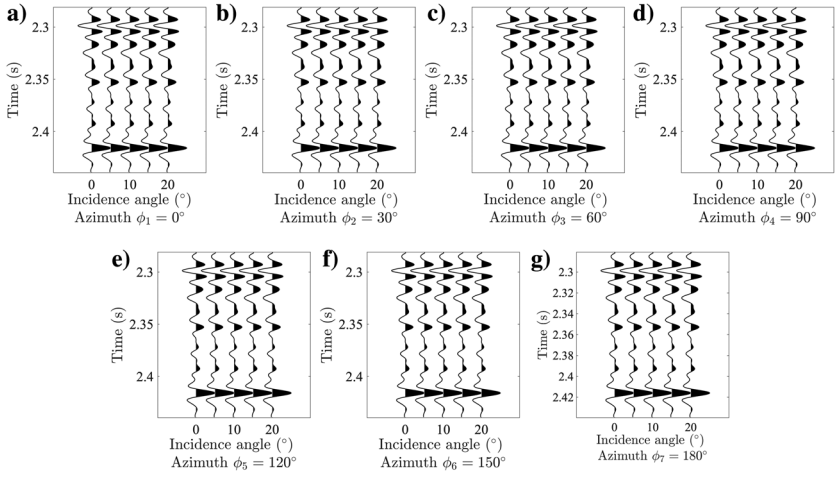

Figure 12. Simulated azimuthal prestack angle gathers by using equation 16.

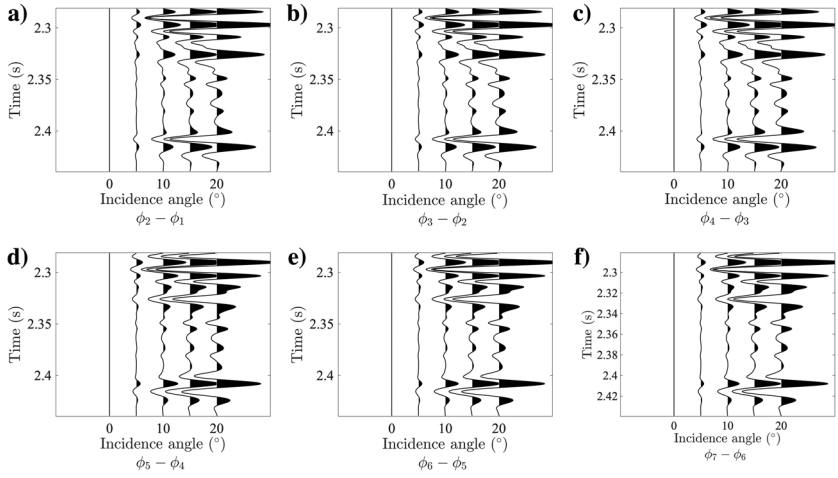

Figure 13. Residual profiles between different azimuthal gathers, where ϕ_i denotes the azimuthal angle ranging from 0° to 180° with 30° intervals.

Because M^b is continuously differentiable along time or depth, under the weak reflection assumption,

$$M^b(t_{i+1}) + M^b(t_i) \approx 2M^b(t_i),$$
$$M^b(t_{i+1}) - M^b(t_i) \approx \frac{dM^b(t_i)}{dt}\Delta t. \tag{53}$$

Then,

$$\mathbf{r}_{M^b}(t) \approx \frac{dM^b}{dt}\frac{1}{2M^b(t)} = \frac{1}{2}\frac{d\ \ln\ M^b}{dt}\Delta t, \tag{54}$$

and

$$M^b(t) = M^b(0)\exp\left(\sum_{i=0}^{N_t}\frac{2\mathbf{r}_{M^b,i}}{\Delta t}\right), \tag{55}$$

where N_t is the temporal sample.

Noise test

The log profiles of Figure 14 are used to evaluate the inversion from different methods in the presence of noise. We test the method with the azimuthal angle-gather data of Figure 12 and different signal-to-noise ratios (S/Ns).

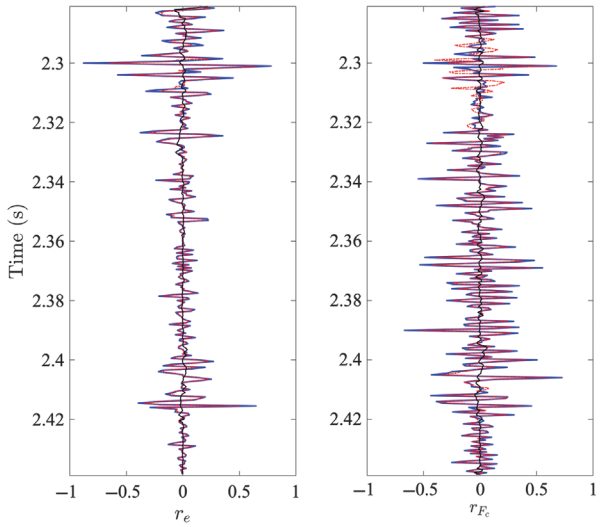

Figure 14. Comparison between the inverted r_e and r_{F_c} (dashed red line) and the well-log data (the solid blue line). The dashed black lines correspond to the initial model.

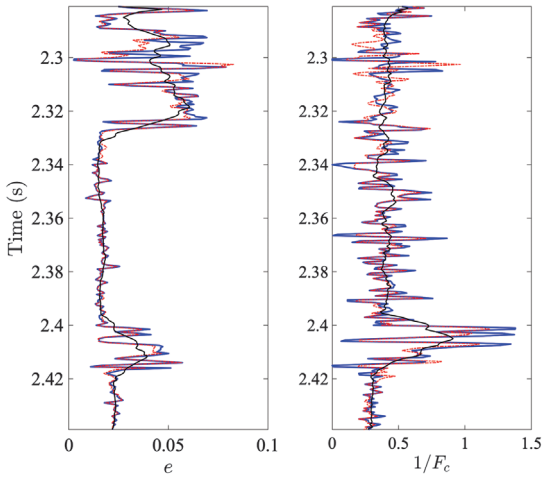

Figure 15. Inverted fracture density e and fracture-fluid indicator $1/F_c$ (the dashed red line) by using a trace integral algorithm on r_e and r_{F_c} and the well-log data (the solid blue line). The dashed black lines correspond to the initial model.

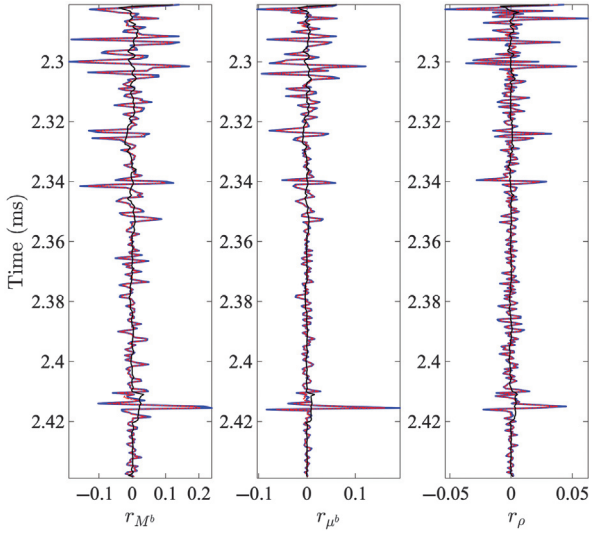

Figure 16. Inverted r_{M^b}, r_{μ^b}, and r_ρ of the background medium (the dashed red line) and the real well-log data (the solid blue line).

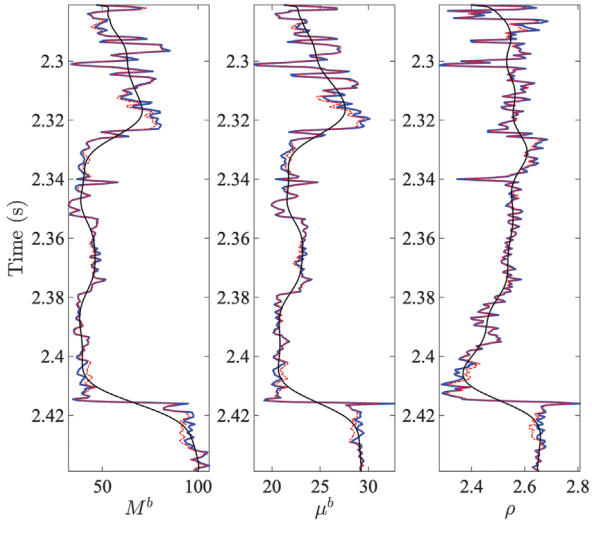

Figure 17. Inverted elastic parameters of the isotropic part of the reflection coefficient by using a trace integral algorithm on r_{M^b}, r_{μ^b}, and r_ρ (the dashed red line) and the real well-log data (the solid blue line).

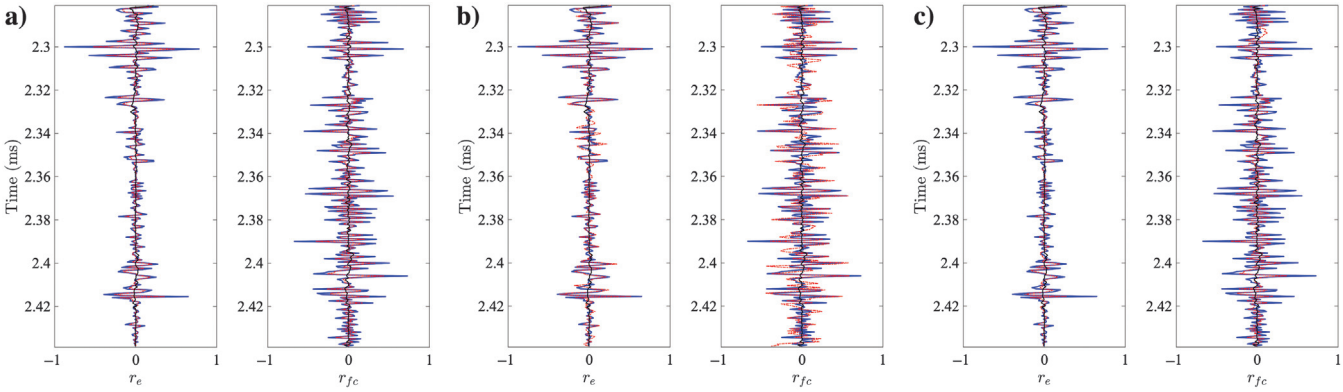

Figure 18. Inverted r_e and r_{F_c} (the dashed red line) and well-log data (the solid blue line) from noise-corrupted seismic data; S/N is (a) 5, (b) 3, and (c) 2.

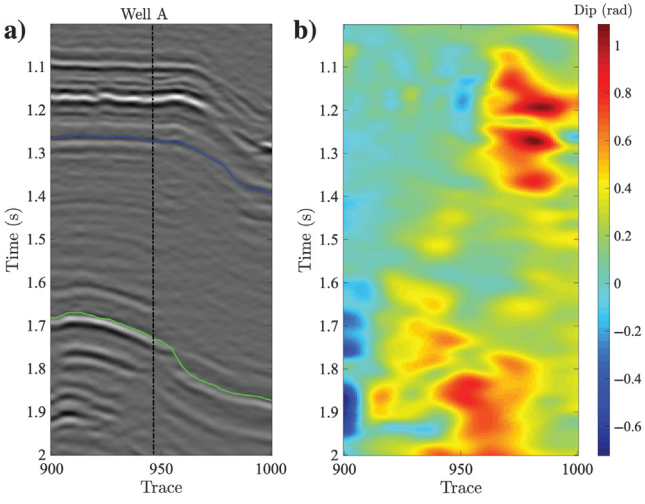

Figure 19. (a) Prestack migrated seismic profile and (b) estimated seismic dip attribute by using the PWD algorithm.

We assume that the random noise has a zero-mean Gaussian distribution. Then, we obtain r_e and r_{F_c} (the dashed red line) with S/N = 5 (Figure 18a), 3 (Figure 18b), and 2 (Figure 18c), as shown in Figure 18. We observe that the inversion works even in the case of a relatively strong noise. The target parameters have a contribution similar to the seismic data. Moreover, the inversion method is affected by many other factors, such as the regularization weight, the optimization method, and the objective function.

REAL-DATA EXAMPLE

The inversion based on the proposed method is performed on seismic data from southwest China. As shown in Figure 19a, the blue and green lines correspond to the top and bottom of a shale formation characterized by a large number of fractures, respectively, as a result of complex tectonic processes. The bottom of the shale reservoir corresponds to the solid green line, and the top of the shale reservoir is located 0.1 s above the solid green line. The shale gas is stored in the shale reservoirs and is the main target of exploration. The data consist of 101 azimuthal angle gathers (common-depth point from 900 to 1000), prestack time migrated, with 1°–30° incidence angles and 0°–150° azimuthal angles.

Sunjay and Kothari (2011) and Chen et al. (2018) neglect the clay lamination properties of the background and it is assumed that

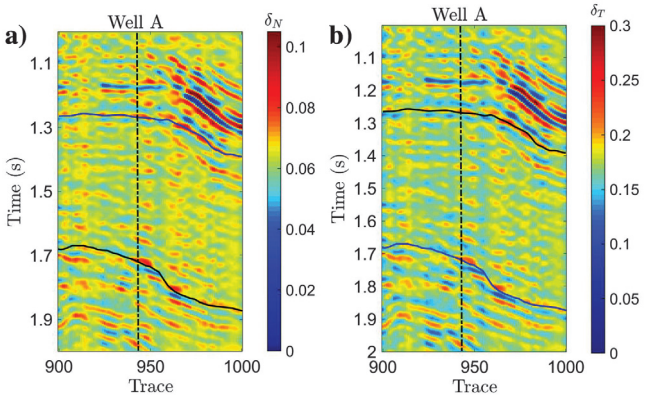

Figure 20. Inverted fracture weakness δ_N and δ_T by using fixed tilt angle $\pi/4$.

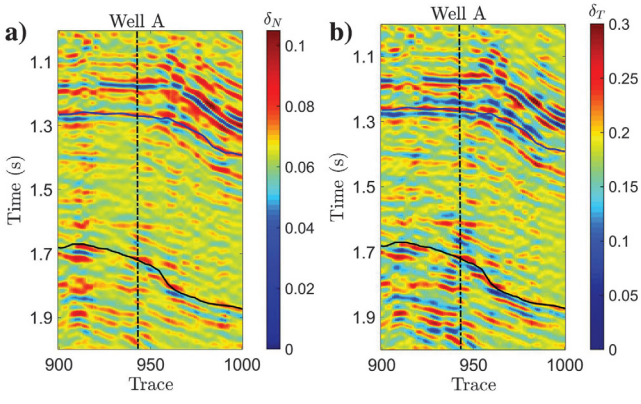

Figure 21. Inverted fracture weakness δ_N and δ_T by using the estimated tilt angle by using the seismic dip angle in Figure 19b.

DOI:10.1190/geo2021-0631.1

the fractures are perpendicular to the dip of the formation, which can be retrieved by plane-wave destruction (PWD) (Claerbout and Abma, 1992; Fomel, 2002). Then, the tilt angle of the TTI media can be obtained. According to Claerbout and Abma (1992), plane waves can be expressed by the first-order differential equation as follows:

$$\frac{\partial u(x,t)}{\partial x} + \varsigma(x,t)\frac{\partial u(x,t)}{\partial t} = 0, \tag{56}$$

where $u(x,t)$ denotes the wavefield and $\varsigma(x,t)$ corresponds to the seismic dip. Figure 19b shows the dip attribute by using this algorithm. The left side of the seismic data is relatively flat, corresponding to HTI media, whereas the right side is severely tilted (TTI media). Thus, we cannot assume a single axis of symmetry.

We first assume that the strata are a set of TTI media with a fixed tilt angle of 45° and use the fracture-weakness-based approximation to perform the inversion. The results are shown in Figure 20, where we can see that a fixed tilt-angle assumption is not applicable to this complex formation. The inversion results exhibit a poor lateral continuity. The fixed tilt angle may cause anomalies ("strip-like" artifacts in the inversion profiles), which are related to the increasing ill-posedness induced by the inaccurate tilt angles. Moreover, the positions highlighted by the block dashed boxes in Figures 20 and 21 show that the energy of inversion results on the right side is stronger than that of the left side. It is not reasonable for the same strata.

Figure 21 shows 2D inversion profiles of fracture weakness by using the PWD-estimated tilt angle. We can see that the inversion has improved considerably, with the left and right sides being relatively even in magnitude. Furthermore, the borehole side inversion results are extracted from Figures 20 and 21. Then, the comparison between the borehole-side inversion results δ_N and δ_T (the dashed red lines) and the well-log data (the solid black lines) is performed, as shown in Figure 22. It is shown that the inversion accuracy with fixed tilt-angle is inferior to that of the proposed method.

Finally, Figure 23 shows the results by using the proposed approximation. We directly extract the fracture density e and fracture-fluid indicator factor F_c from the seismic data. As shown in Figure 23b, the proposed fluid indicator, which is proportional to the fluid bulk modulus, is well adapted to shale gas reservoirs. To further verify the effectiveness of the proposed method, Figure 24 compares e (Figure 24a) and F_c (Figure 24c) with permeability and water saturation well-log profiles. Permeability provides an indication of the fractures, with a high value corresponding to a high fracture density, and low water saturation indicates high gas content (low bulk modulus of the fluid). The comparison between the synthetic data generated by using the inversion results and the real data is performed. Figure 25a and 25b shows the real and synthetic angle gathers at 90° azimuth angle, respectively, and Figure 25c

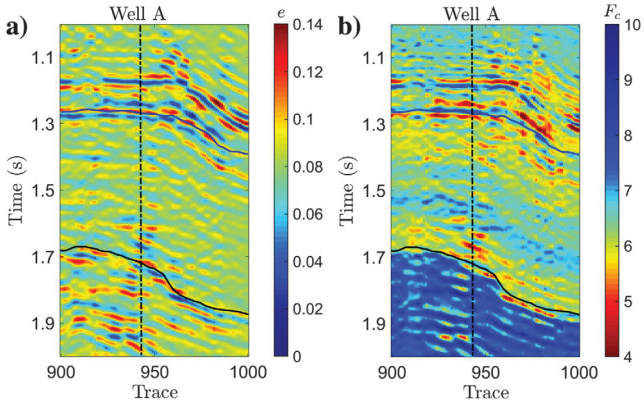

Figure 23. Inverted fracture density e and fracture-fluid indicator F_c by using the proposed approximation.

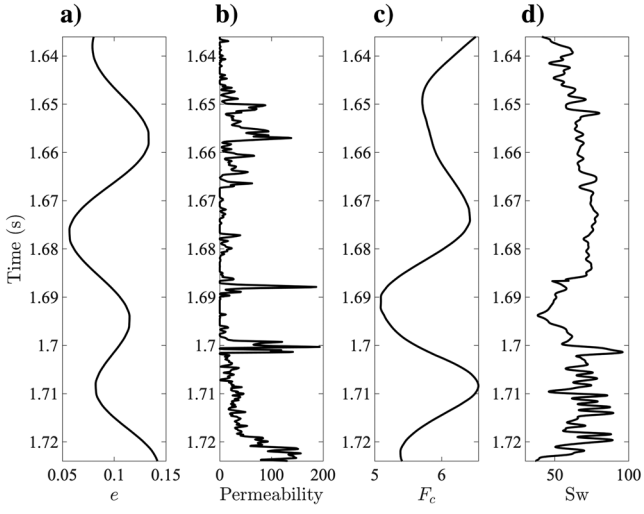

Figure 24. (a) The inverted fracture density e, (b) permeability well-log curve, (c) the inverted fluid indicator in cracks F_c, and (d) water saturation well-log curve.

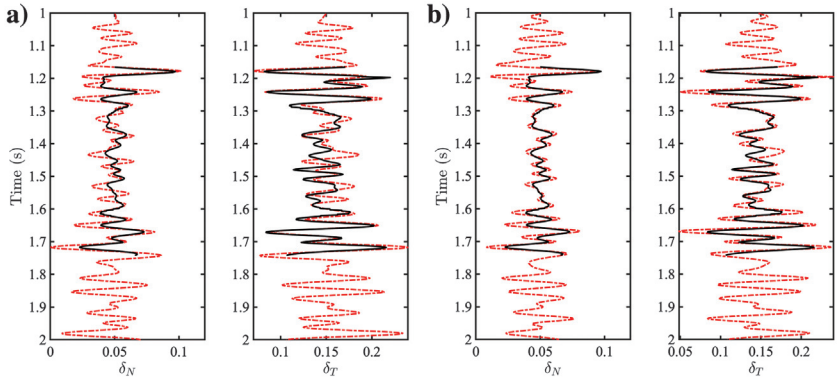

Figure 22. Comparison between the borehole-side inversion results δ_N and δ_T (the dashed red lines) and smoothed well-log data (the solid black lines).

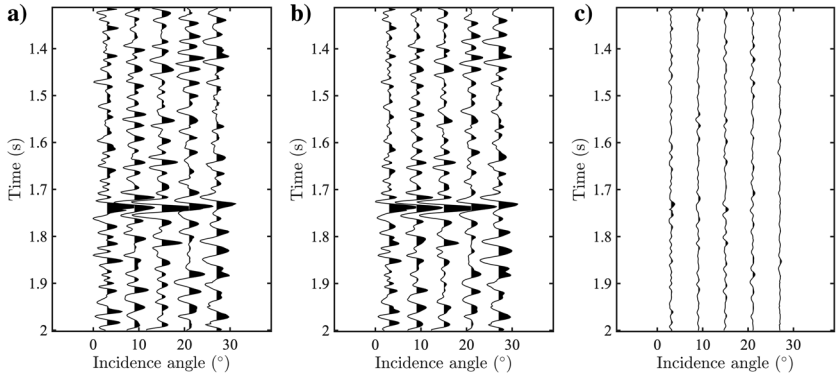

Figure 25. Comparison between (a) the real and (b) the synthetic data at 90° azimuth angle by using the inversion results, and (c) the residual profile between them.

corresponds to the residual profile of the two angle gathers. This example demonstrates that the proposed method can be adopted for fractured reservoir characterization and fluid detection.

DISCUSSION

AVAZ inversion is currently an effective method for quantitative characterization of anisotropic media, especially fractured media. However, this method can be conducted only in weak-contrast and weak-anisotropic media.

The determination of the tilt angle of TTI media is difficult to estimate. Here, we assume that the fractures are perpendicular to the dip of the formation, which can be retrieved by PWD.

Thin coin-shaped fracture and linear-slip models are adopted to decouple the effects of the fractures and saturating fluid. We have defined an indicator to characterize the fluid and neglect the effect of the fracture aspect ratio. This drawback needs further investigation and the indicator can be generalized to retrieve the fracture properties from azimuthal seismic data. Moreover, the seismic response of the fractured medium can be improved by using wave-induced fluid-flow theories, which describe attenuation and dispersion (Carcione et al., 2013). AVAZ inversion can be generalized to the anelastic case for a better characterization of the seismic response of the reservoir.

CONCLUSION

We have proposed a rock matrix-fracture-fluid decoupled PP-wave reflection coefficient approximation of a weakly TTI medium for AVAZ inversion. Compared with the conventional fracture-weakness-based approximation, the proposed method incorporates the fracture density and a fluid indicator. Moreover, the anisotropic part of the approximation yields a more balanced parameter contribution (or sensitivity) to the seismic data, which reduces the ill-posedness of the corresponding inverse problem. In the inversion process, an initial model can be provided and iteratively updated, so that the final result is optimal. The inversion test shows that the method is feasible and can be applied to real data.

ACKNOWLEDGMENTS

This work was supported in part by the National Natural Science Foundation of China under Grant 42004111, in part by Jiangsu Innovation and Entrepreneurship Plan, and in part by Jiangsu Province Science Fund for Distinguished Young Scholars.

DATA AND MATERIALS AVAILABILITY

Data associated with this research are available and can be obtained by contacting the corresponding author.

APPENDIX A

SLOWNESS AND WAVE VECTORS

For P waves propagating in a TI medium, the wave vectors of the incident and reflection waves on an interface are, respectively,

$$\begin{aligned}\mathbf{t} &= [\sin\theta\cos\phi, \sin\theta\sin\phi, \cos\theta],\\ \mathbf{t}' &= [-\sin\theta\cos\phi, -\sin\theta\sin\phi, \cos\theta],\end{aligned} \tag{A-1}$$

and the corresponding slowness vectors are

$$\begin{aligned}\mathbf{p} &= \frac{1}{\alpha^b}[\sin\theta\cos\phi, \sin\theta\sin\phi, \cos\theta],\\ \mathbf{p}' &= \frac{1}{\alpha^b}[-\sin\theta\cos\phi, -\sin\theta\sin\phi, \cos\theta].\end{aligned} \tag{A-2}$$

Moreover,

$$\xi = t_i t_i'|_{r=r_0} = \cos 2\theta, \tag{A-3}$$

and

$$\eta_{ij} = t_i' p_j' t_k p_l|_{r=r_0}, \tag{A-4}$$

where η_{ij} are the components of matrix $\mathbf{E}$, which is

$$\mathbf{E} = \frac{1}{(\alpha^b)^2}\begin{bmatrix}
\sin^4\theta\cos^4\phi & \sin^4\theta\sin^2\phi\cos^2\phi & \sin^2\theta\cos^2\theta\cos^2\phi & 2\sin^3\theta\cos\theta\sin\phi\cos^2\phi & -2\sin^3\theta\cos\phi\cos^3\phi & 2\sin^4\theta\sin\phi\cos^3\phi\\
\sin^4\theta\sin^2\theta\cos^2\phi & \sin^4\theta\sin^4\phi & \sin^2\theta\cos^2\theta\sin^2\phi & -2\sin^3\theta\cos\theta\sin^3\phi & -2\sin^3\theta\cos\theta\sin^2\phi\cos\phi & 2\sin^4\theta\sin^3\phi\cos\phi\\
\sin^2\theta\cos^2\theta\cos^2\phi & \sin^2\theta\cos^2\theta\sin^2\phi & \cos^4\theta & 2\sin\theta\cos^3\theta\sin\phi & -2\sin\theta\cos^3\theta\cos\phi & 2\sin^2\theta\cos^2\theta\sin\phi\cos\phi\\
-2\sin^3\theta\cos\theta\sin\phi\cos^2\phi & 2\sin^3\theta\cos\theta\sin^3\phi & -2\sin\theta\cos^3\theta\sin\phi & -4\sin^2\theta\cos^2\theta\sin^2\phi & -4\sin^2\theta\cos^2\theta\sin\phi\cos\phi & -4\sin^3\theta\cos\theta\sin^2\phi\cos\phi\\
2\sin^3\theta\cos\theta\cos^3\phi & 2\sin^3\theta\cos\theta\sin^2\phi\cos\phi & 2\sin\theta\cos^3\theta\cos\phi & -4\sin^2\theta\cos^2\theta\sin\phi\cos\phi & -4\sin^2\theta\cos^2\theta\cos^2\phi & -4\sin^3\theta\cos\theta\sin\phi\cos^2\phi\\
2\sin^4\theta\sin\phi\cos^3\phi & 2\sin^4\theta\sin^3\phi\cos\phi & 2\sin^2\theta\cos^2\theta\sin\phi\cos\phi & 4\sin^3\theta\cos\theta\sin^2\phi\cos\phi & 4\sin^3\theta\cos\theta\sin\phi\cos^2\phi & 4\sin^4\theta\sin^2\phi\cos^2\phi
\end{bmatrix}. \tag{A-5}$$

Then, substituting equations B-3, A-4, and A-5 into equation 8, we obtain $R_{\mathrm{PP}}^{\mathrm{ani}}$.

APPENDIX B

STIFFNESS COEFFICIENTS OF TTI MEDIA AND PERTURBATION TERMS

The stiffness coefficients for TTI media are

$$
\begin{aligned}
c_{11} &= (c_{11}^v \cos^2\theta_0 + c_{13}^v \sin^2\theta_0)\cos^2\theta_0 \\
&\quad + (c_{13}^v \cos^2\theta_0 + c_{33}^v \sin^2\theta_0)\sin^2\theta_0 + \sin^2 2\theta_0 c_{55}^v, \\
c_{12} &= c_{12}^v \cos^2\theta_0 + c_{13}^v \sin\theta_0, \\
c_{13} &= (c_{11}^v \cos^2\theta_0 + c_{13}^v \sin^2\theta_0)\sin^2\theta_0 \\
&\quad + (c_{13}^v \cos^2\theta_0 + c_{33}^v \sin^2\theta_0)\cos^2\theta_0 - \sin^2 2\theta_0 c_{55}^v, \\
c_{15} &= \frac{1}{2}(c_{11}^v \cos^2\theta_0 + c_{13}^v \sin^2\theta_0)\sin 2\theta_0 - \frac{1}{2}(c_{13}^v \cos^2\theta_0 \\
&\quad + c_{33}^v \sin^2\theta_0)\sin 2\theta_0 - c_{55}^v \sin 2\theta_0 \cos 2\theta_0, \\
c_{22} &= c_{11}^v, \\
c_{23} &= c_{12}^v \sin^2\theta_0 + c_{13}^v \cos^2\theta_0, \\
c_{25} &= \frac{1}{2}c_{12}^v \sin^2 2\theta_0 - \frac{1}{2}c_{13}^v \sin^2 2\theta_0, \\
c_{33} &= (c_{11}^v \sin^2\theta_0 + c_{13}^v \cos^2\theta_0)\sin^2\theta_0 \\
&\quad + (c_{13}^v \sin^2\theta_0 + c_{33}^v \cos^2\theta_0)\cos^2\theta_0 + \sin^2 2\theta_0 c_{55}^v, \\
c_{35} &= \frac{1}{2}(c_{11}^v \sin^2\theta_0 + c_{13}^v \cos^2\theta_0)\sin 2\theta_0 - \frac{1}{2}(c_{13}^v \sin^2\theta_0 \\
&\quad + c_{33}^v \cos^2\theta_0)\sin 2\theta_0 + c_{55}^v \sin 2\theta_0 \cos 2\theta_0, \\
c_{44} &= c_{55}^v \cos^2\theta_0 + c_{66}^v \sin^2\theta_0, \\
c_{46} &= -\frac{1}{2}c_{55}^v \sin 2\theta_0 + \frac{1}{2}c_{66}^v \sin 2\theta_0, \\
c_{55} &= -\frac{1}{4}(c_{11}^v \sin 2\theta_0 - c_{13}^v \sin 2\theta_0)\sin 2\theta_0 \\
&\quad - \frac{1}{4}(c_{13}^v \sin 2\theta_0 - c_{33}^v \sin 2\theta_0)\sin 2\theta_0 + c_{55}^v \cos^2 2\theta_0, \\
c_{66} &= c_{55}^v \sin^2\theta_0 + c_{66}^v \cos^2\theta_0. \qquad \text{(B-1)}
\end{aligned}
$$

Substituting equation 11 into equation B-1, we obtain

$$
\begin{aligned}
c_{11} &= M^b + \sin^2 2\theta_0 \mu^b \delta_T \\
&\quad - [M^b(\sin^4\theta_0 + (\gamma^b)^2\cos^4\theta_0) - \frac{1}{2}\lambda^b \sin^2 2\theta_0]\delta_N, \\
c_{12} &= \lambda^b[1 - \delta_N(\gamma^b \cos^2\theta_0 + \sin^2\theta_0)], \\
c_{13} &= \lambda^b(1-\delta_N) + \frac{1}{4}[2\lambda^b\delta_N - M^b\delta_N(1 + (\gamma^b)^2)\sin^2 2\theta_0 + 4\mu^b\delta_T], \\
c_{15} &= \frac{1}{4}(\lambda^b\delta_N + 2\mu^b\delta_T)\sin 4\theta_0 + \frac{1}{2}[M^b\delta_N(\sin^2\theta_0 - \gamma^b\cos^2\theta_0)]\sin 2\theta_0, \\
c_{22} &= M^b(1 - (\gamma^b)^2\delta_N), \\
c_{23} &= \lambda^b[1 - \delta_N(\gamma^b \sin^2\theta_0 + \cos^2\theta_0)], \\
c_{25} &= \frac{1}{2}[\lambda^b(1-\gamma^b)]\delta_N \sin 2\theta_0, \\
c_{33} &= M^b - \sin^2 2\theta_0 \mu^b \delta_T \\
&\quad - \left[M^b(\cos^4\theta_0 + (\gamma^b)^2\sin^4\theta_0) + \frac{1}{2}\lambda^b \sin^2 2\theta_0\right]\delta_N, \\
c_{35} &= -\frac{1}{2}\left[M^b\delta_N((\gamma^b)^2\sin^2\theta_0 + \cos^2\theta_0)] + \frac{1}{4}[2\mu^b\delta_T - \lambda^b\delta_N\right]\sin^4\theta_0, \\
c_{44} &= \mu^b(1 - \delta_T \cos^2\theta_0), \quad c_{46} = \frac{1}{2}\mu^b\delta_T \sin 2\theta_0, \\
c_{55} &= \mu^b - \frac{1}{4}[2\lambda^b + M^b((\gamma^b)^2 + 1)]\sin^2 2\theta\delta_N - \mu^b \cos^2 2\theta_0\delta_T, \\
c_{66} &= \mu^b(1 - \delta_T \sin^2\theta_0). \qquad \text{(B-2)}
\end{aligned}
$$

According to equation 1, the components of the perturbation term $\Delta\mathbf{C}$ are

$$
\begin{aligned}
\Delta c_{11} &= c_{11} - c_{11}^b \\
&= -\sin^2 2\theta_0\mu^b\Delta\delta_T - [M^b(\sin^4\theta_0 + (\gamma^b)^2\cos^4\theta_0) - \frac{1}{2}\lambda^b\sin^2 2\theta_0]\delta_N, \\
\Delta c_{12} &= c_{12} - c_{12}^b = -(\gamma^b\cos^2\theta_0 + \sin^2\theta_0)\lambda^b\delta_N, \\
\Delta c_{13} &= c_{13} - c_{13}^b = \sin^2 2\theta_0\mu^b\delta_T \\
&\quad + \left[\left(\frac{1}{2}\sin^2 2\theta - 1\right)\lambda^b - \frac{1}{4}(1 + (\gamma^b)^2)\sin^2 2\theta_0\right]\delta_N, \\
\Delta c_{15} &= c_{15} - c_{15}^b = \frac{1}{2}\sin 4\theta_0\mu^b\delta_T \\
&\quad + \left[\frac{1}{2}\sin 2\theta_0(\sin^2\theta_0 - (\gamma^b)^2\cos^2\theta_0)M^b + \frac{1}{4}\lambda^b \sin 4\theta_0\right]\delta_N \\
\Delta c_{22} &= c_{22} - c_{22}^b = -(\gamma^b)^2 M^b\delta_N, \\
\Delta c_{23} &= c_{23} - c_{23}^b = -(\cos^2\theta_0 + \gamma^b\sin^2\theta_0)\lambda^b\delta_N, \\
\Delta c_{25} &= c_{25} - c_{25}^b = \frac{1}{2}[\lambda^b(1-\gamma^b)]\sin 2\theta_0\delta_N, \\
\Delta c_{33} &= c_{33} - c_{33}^b = -\sin^2 2\theta_0\mu^b\delta_T \\
&\quad - [M^b(\cos^4\theta_0 + (\gamma^b)^2\sin^4\theta_0) + \frac{1}{2}\lambda^b\sin^2 2\theta_0]\delta_N, \\
\Delta c_{35} &= c_{35} - c_{35}^b = -\frac{1}{2}\mu^b \sin 4\theta_0\delta_T - \frac{1}{4}(2M^b(\gamma^b)^2\sin^2\theta_0 \\
&\quad + 2M^b\cos^2\theta_0 - \lambda^b\sin 4\theta_0)\delta_N, \\
\Delta c_{44} &= c_{44} - c_{44}^b = -\mu^b\cos^2\theta_0\delta_T, \\
\Delta c_{46} &= c_{46} - c_{46}^b = \frac{1}{2}\sin 2\theta_0\mu^b\delta_T, \\
\Delta c_{55} &= c_{55} - c_{55}^b = -\mu^b\cos^2 2\theta_0\delta_T \\
&\quad - \frac{1}{4}[2\lambda^b + M^b((\gamma^b)^2 + 1)]\sin^2 2\theta\delta_N, \\
\Delta c_{66} &= c_{66} - c_{66}^b = -\mu^b\sin^2\theta_0\delta_T. \qquad \text{(B-3)}
\end{aligned}
$$

REFERENCES

Aki, K., and P. G. Richard, 1980, Quantitative seismology: Theory and methods: W. H. Freeman.

Alemie, W., and M. D. Sacchi, 2011, High-resolution three-term AVO inversion by means of a Trivariate Cauchy probability distribution: Geophysics, **76**, no. 3, R43–R55, doi: 10.1190/1.3554627.

Ba, J., W. Xu, L. Fu, J. M. Carcione, and L. Zhang, 2017, Rock anelasticity due to patchy saturation and fabric heterogeneity: A double double-porosity model of wave propagation: Journal of Geophysical Research: Solid Earth, **122**, 1949–1976, doi: 10.1002/2016JB013882.

Bachrach, R., M. Sengupta, A. Salama, and P. Miller, 2009, Reconstruction of the layer anisotropic elastic parameters and high-resolution fracture characterization from P-wave data: A case study using seismic inversion and Bayesian rock physics parameter estimation: Geophysical Prospecting, **57**, 253–262, doi: 10.1111/j.1365-2478.2008.00768.x.

Bakulin, A., V. Grechka, and I. Tsvankin, 2000a, Estimation of fracture parameters from reflection seismic data — Part I: HTI model due to a single fracture set: Geophysics, **65**, 1788–1802, doi: 10.1190/1.1444863.

Bakulin, A., V. Grechka, and I. Tsvankin, 2000b, Estimation of fracture parameters from reflection seismic data — Part II: Fractured models with orthorhombic symmetry: Geophysics, **65**, 1803–1817, doi: 10.1190/1.1444864.

Behura, J., and I. Tsvankin, 2006, Small-angle AVO response of PS-waves in tilted transversely isotropic media: Geophysics, **71**, no. 5, C69–C79, doi: 10.1190/1.2329865.

Bond, W. L., 1943, The mathematics of the physical properties of crystals: The Bell System Technical Journal, **22**, 1–72, doi: 10.1002/j.1538-7305.1943.tb01304.x.

Burridge, R., M. V. de Hoop, D. Miller, and C. Spencer, 1998, Multiparameter inversion in anisotropic elastic media: Geophysical Journal International, **134**, 757–777, doi: 10.1046/j.1365-246x.1998.00590.x.
Carcione, J. M., 2014, Wave fields in real media. Theory and numerical simulation of wave propagation in anisotropic, anelastic, porous and electromagnetic media, 3rd ed.: Elsevier Science.
Carcione, J. M., B. Gurevich, J. E. Santos, and S. Picotti, 2013, Angular and frequency dependent wave velocity and attenuation in fractured porous media: Pure and Applied Geophysics, **170**, 1673–1683, doi: 10.1007/s00024-012-0636-8.
Carcione, J. M., and S. Picotti, 2012a, Reflection and transmission coefficients of a fracture in transversely isotropic media: Studia Geophysica et Geodaetica, **56**, 307–322, doi: 10.1007/s11200-011-9034-4.
Carcione, J. M., S. Picotti, and J. E. Santos, 2012b, Numerical experiments of fracture induced velocity and attenuation anisotropy: Geophysical Journal International, **191**, 1179–1191, doi: 10.1111/j.1365-246X.2012.05697.x.
Carcione, J. M., J. E. Santos, and S. Picotti, 2012c, Fracture-induced anisotropic attenuation: Rock Mechanics and Rock Engineering, **45**, 929–942, doi: 10.1007/s00603-012-0237-y.
Cerveny, V., 2001, Seismic ray theory: Cambridge University Press.
Chapman, C. H., and R. T. Coates, 1994, Generalized Born scattering in anisotropic media: Wave Motion, **19**, 309–341, doi: 10.1016/0165-2125(94)90001-9.
Chen, H., T. Chen, and K. A. Innanen, 2020, Estimating tilted fracture weaknesses from azimuthal differences in seismic amplitude data: Geophysics, **85**, no. 3, R135–R146, doi: 10.1190/geo2019-0344.1.
Chen, H., Y. Ji, and K. A. Innanen, 2018, Estimation of modified fluid factor and dry fracture weaknesses using azimuthal elastic impedance: Geophysics, **83**, no. 1, WA73–WA88, doi: 10.1190/geo2017-0075.1.
Chen, H., X. Pan, Y. Ji, and G. Zhang, 2017, Bayesian Markov chain Monte Carlo inversion for weak anisotropy parameters and fracture weaknesses using azimuthal elastic impedance: Geophysical Journal International, **210**, 801–818, doi: 10.1093/gji/ggx196.
Chen, H., X. Yin, C. Gao, G. Zhang, and J. Chen, 2014, AVAZ inversion for fluid factor based on fractured anisotropic rock physics theory: Chinese Journal of Geophysics, **57**, 968–978, doi: 10.6038/cjg20140326.
Chen, H., X. Yin, J. Gao, B. Liu, and G. Zhang, 2015, Seismic inversion for underground fractures detection based on effective anisotropy and fluid substitution: Science China Earth Sciences, **58**, 805–814, doi: 10.1007/s11430-014-5022-1.
Claerbout, J. F., and R. Abma, 1992, Earth soundings analysis: Processing versus inversion: Blackwell Scientific Publications.
Crampin, S., 1984, Effective anisotropic elastic constants for wave propagation through cracked solids: Geophysical Journal International, **76**, 135–145, doi: 10.1111/j.1365-246X.1984.tb05029.x.
Daley, P. F., and F. Hron, 1977, Reflection and transmission coefficients for transversely isotropic media: Bulletin of the Seismological Society of America, **67**, 661–675, doi: 10.1785/BSSA0670030661.
Domenico, S. N., 1976, Effect of brine-gas mixture on velocity in an unconsolidated sand reservoir: Geophysics, **41**, 882–894, doi: 10.1190/1.1440670.
Eaton, D. W., and R. R. Stewart, 1994, Migration/inversion for transversely isotropic elastic media: Geophysical Journal International, **119**, 667–683, doi: 10.1111/j.1365-246X.1994.tb00148.x.
Fomel, S., 2002, Applications of plane-wave destruction filters: Geophysics, **67**, 1946–1960, doi: 10.1190/1.1527095.
Gassmann, F., 1951, Elastische Wellen in porösen Medien: Zeitschrift für angewandte Mathematik und Physik, **1**, 144–147, doi: 10.1007/BF02009325.
Graebner, M., 1992, Plane-wave reflection and transmission coefficients for a transversely isotropic solid: Geophysics, **57**, 1512–1519, doi: 10.1190/1.1443219.
Gray, D., P. Anderson, J. Logel, F. Delbecq, D. Schmidt, and R. Schmid, 2012, Estimation of stress and geomechanical properties using 3D seismic data: First Break, **30**, 59–68, doi: 10.3997/1365-2397.2011042.
Henneke, E. G., 1972, Reflection-refraction of a stress wave at a plane boundary between anisotropic media: The Journal of the Acoustical Society of America, **51**, 210–217, doi: 10.1121/1.1912832.
Hornby, B. E., L. M. Schwartz, and J. A. Hudson, 1994, Anisotropic effective-medium modeling of the elastic properties of shales: Geophysics, **59**, 1570–1583, doi: 10.1190/1.1443546.
Hsu, C. J., and M. Schoenberg, 1993, Elastic waves through a simulated fractured medium: Geophysics, **58**, 964–977, doi: 10.1190/1.1443487.
Huang, G., X. Chen, C. Luo, and X. Li, 2019, Prestack waveform inversion by using an optimized linear inversion scheme: IEEE Transactions on Geoscience and Remote Sensing, **57**, 5716–5728, doi: 10.1109/TGRS.2019.2901725.
Hudson, J. A., 1981, Wave speeds and attenuation of elastic waves in material containing cracks: Geophysical Journal International, **64**, 133–150, doi: 10.1111/j.1365-246X.1981.tb02662.x.
Ivanov, Y., and A. Stovas, 2017, Weak-anisotropy approximation for P-wave reflection coefficient at the boundary between two tilted transversely isotropic media: Geophysical Prospecting, **65**, 485–502, doi: 10.1111/1365-2478.12436.
Jílek, P., 2002, Converted PS-wave reflection coefficients in weakly anisotropic media: Pure and Applied Geophysics, **159**, 1527–1562, doi: 10.1007/s00024-002-8696-9.
Jin, S., and A. Stovas, 2020, S-wave in 2D acoustic transversely isotropic media with a tilted symmetry axis: Geophysical Prospecting, **68**, 483–500, doi: 10.1111/1365-2478.12856.
Keith, C. M., and S. Crampin, 1977, Seismic body waves in anisotropic media: Reflection and refraction at a plane interface: Geophysical Journal International, **49**, 181–208 doi: 10.1111/j.1365-246X.1977.tb03708.x.
Liang, K., X. Yin, and G. Wu, 2011, Exact and approximate reflection and transmission coefficient for incident qP wave in TTI media: Chinese Journal of Geophysics, **54**, 208–217, doi: 10.3969/j.issn.0001-5733.2011.01.022.
Liu, C. X., X. Wang, X. Zhang, J. Mo, D. Wang, G. Wei, and F. Pan, 2020, Open fracture detection from the new-generation oil-based microresistivity image logs: A case study from the Bashijiqike sandstone, Tarim Basin of China: International Petroleum Technology Conference.
Luo, C., J. Ba, J. M. Carcione, G. Huang, and Q. Guo, 2020, Joint PP and PS pre-stack AVA inversion for VTI medium based on the exact Graebner equation: Journal of Petroleum Science and Engineering, **194**, 107416, doi: 10.1016/j.petrol.2020.107416.
Luo, C., G. Huang, X. Chen, and Y. Chen, 2021, Registration-free multicomponent joint AVA inversion using optimal transport: IEEE Transactions on Geoscience and Remote Sensing, **60**, 1–13, doi: 10.1109/TGRS.2021.3063271.
Narr, W., 1991, Fracture density in the deep subsurface: Techniques with application to Point Arguello oil field: AAPG Bulletin, **75**, 1300–1323, doi: 10.1306/0C9B2939-1710-11D7-8645000102C1865D.
Oh, J. W., and T. Alkhalifah, 2016, The scattering potential of partial derivative wave-fields in 3-D elastic orthorhombic media: An inversion prospective: Geophysical Journal International, **206**, 1740–1760, doi: 10.1093/gji/ggw238.
Pan, X., L. Li, S. Zhou, G. Zhang, and J. Liu, 2021, Azimuthal amplitude variation with offset parameterization and inversion for fracture weaknesses in tilted transversely isotropic media: Geophysics, **86**, no. 1, C1–C18, doi: 10.1190/geo2019-0215.1.
Pan, X., G. Zhang, and X. Yin, 2018, Azimuthally pre-stack seismic inversion for orthorhombic anisotropy driven by rock physics: Science China, Earth Sciences, **61**, 425–440, doi: 10.1007/s11430-017-9124-6.
Pan, X., G. Zhang, and X. Yin, 2019a, Amplitude variation with offset and azimuth inversion for fluid indicator and fracture weaknesses in an oil-bearing fractured reservoir: Geophysics, **84**, no. 3, N41–N53, doi: 10.1190/geo2018-0554.1.
Pan, X., G. Zhang, and X. Yin, 2019b, Linearized amplitude variation with offset and azimuth and anisotropic poroelasticity: Geophysical Prospecting, **67**, 1882–1897, doi: 10.1111/1365-2478.12778.
Pan, X., G. Zhang, and X. Yin, 2021, Azimuthal amplitude variation with offset parameterization and inversion for fracture weaknesses in tilted transversely isotropic media: Geophysics, **86**, no. 1, C1–C18, doi: 10.1190/GEO2019-0215.1.
Rüger, A., 1997, P-wave reflection coefficients for transversely isotropic models with vertical and horizontal axis of symmetry: Geophysics, **62**, 713–722, doi: 10.1190/1.1444181.
Rüger, A., 1998, Variation of P-wave reflectivity with offset and azimuth in anisotropic media: Geophysics, **63**, 935–947, doi: 10.1190/1.1444405.
Rüger, A., 2002, Reflection coefficients and azimuthal AVO analysis in anisotropic media: SEG.
Russell, B. H., D. Gray, and D. P. Hampson, 2011, Linearized AVO and poroelasticity: Geophysics, **76**, no. 3, C19–C29, doi: 10.1190/1.3555082.
Schoenberg, M., and J. Protazio, 1990, "Zoeppritz" rationalized, and generalized to anisotropic media: The Journal of the Acoustical Society of America, **88**, S46, doi: 10.1121/1.2029011.
Schoenberg, M., and C. M. Sayers, 1995, Seismic anisotropy of fractured rock: Geophysics, **60**, 204–211, doi: 10.1190/1.1443748.
Shaw, R. K., and M. K. Sen, 2004, Born integral, stationary phase and linearized reflection coefficients in weak anisotropic media: Geophysical Journal International, **158**, 225–238, doi: 10.1111/j.1365-246X.2004.02283.x.
Shaw, R. K., and M. K. Sen, 2006, Use of AVOA data to estimate fluid indicator in a vertically fractured medium: Geophysics, **71**, no. 3, C15–C24, doi: 10.1190/1.2194896.
Smith, G. C., and P. M. Gidlow, 1987, Weighted stacking for rock property estimation and detection of gas: Geophysical Prospecting, **35**, 993–1014, doi: 10.1111/j.1365-2478.1987.tb00856.x.
Sunjay, B., and N. Kothari, 2011, An unconventional energy resources: Shale gas: The Offshore Mediterranean Conference and Exhibition.
Wang, H., S. Peng, and W. Du, 2017, Azimuthal AVO for tilted TI medium: Geophysics, **82**, no. 1, C21–C33, doi: 10.1190/geo2015-0430.1.
Wright, J., 1987, The effects of transverse isotropy on reflection amplitude versus offset: Geophysics, **52**, 564–567, doi: 10.1190/1.1442325.
Zhang, L., J. Ba, and J. M. Carcione, 2021, Wave propagation in infinituple-porosity media: Journal of Geophysical Research: Solid Earth, **126**, e2020JB021266, doi: 10.1029/2020JB021266.
Zhang, L., J. Ba, J. M. Carcione, and C. Wu, 2022, Seismic wave propagation in partially saturated rocks with a fractal distribution of fluid-patch size: Journal of Geophysical Research: Solid Earth, **127**, e2021JB023809, doi: 10.1029/2021JB023809.

Biographies and photographs of the authors are not available.